Esra SÜMER LOW DOSE CT IMAGING FOR CANCER DIAGNOSIS AND THERAPY AGU 2018

LOW DOSE CT IMAGING FOR CANCER DIAGNOSIS AND THERAPY

A THESIS
SUBMITTED TO THE DEPARTMENT OF ELECTRICAL AND COMPUTER ENGINEERING
AND THE GRADUATE SCHOOL OF ENGINEERING AND SCIENCE
OF ABDULLAH GUL UNIVERSITY
IN PARTIAL FULFILLMENT OF THE REQUIREMENTS
FOR THE DEGREE OF
M.Sc.

By
Esra SÜMER
June 2018

LOW DOSE CT IMAGING FOR CANCER DIAGNOSIS AND THERAPY

A THESIS
SUBMITTED TO THE DEPARTMENT OF ELECTRICAL AND COMPUTER ENGINEERING
AND THE GRADUATE SCHOOL OF ENGINEERING AND SCIENCE OF ABDULLAH GUL UNIVERSITY
IN PARTIAL FULFILLMENT OF THE REQUIREMENTS
FOR THE DEGREE OF
M.Sc.

By
Esra SÜMER
June 2018

SCIENTIFIC ETHICS COMPLIANCE

I hereby declare that all information in this document has been obtained in accordance with academic rules and ethical conduct. I also declare that, as required by these rules and conduct, I have fully cited and referenced all materials and results that are not original to this work.

Name-Surname: Esra SÜMER
Signature:

REGULATORY COMPLIANCE

M.Sc. thesis titled Low Dose CT Imaging for Cancer Diagnosis and Therapy has been prepared in accordance with the Thesis Writing Guidelines of the Abdullah Gül University, Graduate School of Engineering & Science.

Prepared By

Esra SÜMER

Advisor

Prof. Dr. Bülent YILMAZ

Second Advisor

Assoc. Prof. Dr. İsa YILDIRIM

Head of the Electrical and Computer Engineering Program

Assoc. Prof. Dr. Vehbi Çağrı GÜNGÖR

ACCEPTANCE AND APPROVAL

M.Sc. thesis titled and prepared by Low Dose CT Imaging for Cancer Diagnosis and Therapy has been accepted by the jury in the Electrical and Computer Engineering Graduate Program at Abdullah Gül University, Graduate School of Engineering & Science.

…….. /…….. / ……..

(Thesis Defense Exam Date)

JURY:

Advisor : Prof. Dr. Bülent YILMAZ

Member: Assoc. Prof. Dr. Semra İÇER

Member: Asst. Prof. Dr. Bekir Hakan AKSEBZECİ

APPROVAL:

The acceptance of this M.Sc. thesis has been approved by the decision of the Abdullah Gül University, Graduate School of Engineering & Science, Executive Board dated ….. /….. / …….. and numbered ……..……. .

…….. /…….. / ……..

Graduate School Dean

Prof. Dr. İrfan ALAN

ABSTRACT

LOW DOSE CT IMAGING FOR CANCER DIAGNOSIS AND THERAPY

Esra SÜMER
M.Sc.
Supervisor: Prof. Dr. Bülent YILMAZ
Co-Supervisor: Assoc. Prof. Dr. İsa YILDIRIM

June 2018

Cancer is a common disease among human population and second leading cause of death. It is well known that diagnosing cancer at early stages is very critical for increasing success of therapy. There have been different imaging modalities used in diagnosing and staging of cancer. One of them is computed tomography (CT) that provides two-dimensional (2D) slices of three-dimensional (3D) object using the series of projections taken around the object. The main limitations of CT are radiation dose and low sensitivity to soft tissue. Firstly, fewer projections can be used to lower dose in CT which causes the reconstruction problem heavily underdetermined. Former studies proposed iterative reconstruction techniques to overcome this problem. The significant weakness of these methods is their computational expensiveness. In the present thesis, this problem is addressed by developing a computationally efficient filtered back projection (FBP) based method using total variation (TV) minimization. 2D modified Shepp-Logan phantom is used for performance evaluations. The superiority of the proposed method is shown both qualitatively and quantitatively. The second aim of the thesis is to enhance contrast capability of CT imaging by using novel magnetic nanoparticles (MNPs) as contrast agents which were fabricated at Mechanical Engineering Department of Istanbul Technical University. The pixel density enhancements of CT images induced by five different core types of MNPs in the agarose gel are analyzed. The results confirm the effectiveness of the MNPs as contrast media for CT imaging.

Keywords: sparse CT, filtered backprojection, total variation, magnetic nanoparticles, contrast enhancement.

ÖZET

KANSER TEŞHİS VE TEDAVİSİ İÇİN DÜŞÜK DOZDA BT GÖRÜNTÜLEME

Esra SÜMER
Elektrik ve Bilgisayar Mühendisliği Bölümü Yüksek Lisans
Tez Yöneticisi: Prof. Dr. Bülent YILMAZ
II. Danışman: Doç. Dr. İsa YILDIRIM
Haziran 2018

Kanser, insanlarda sıkça görülen ve ölüm sebepleri arasında ikinci sırada olan bir hastalıktır. Kanserin erken evrelerde teşhis edilmesinin tedavinin başarısını arttırmak için çok kritik olduğu bilinmektedir. Kanserin teşhisi ve evresinin belirlenmesinde farklı görüntüleme yöntemleri kullanılır. Bu yöntemlerden biri bilgisayarlı tomografi (BT), nesnenin etrafından alınan iz düşümleri kullanarak üç boyutlu (3B) nesnenin iki boyutlu (2B) görüntü dilimlerini sağlar. BT'nin temel kısıtları radyasyon dozu ve düşük kontrast duyarlılığıdır. Öncelikle, BT'de radyasyon dozunu azaltmak için daha az sayıda iz düşüm alınabilir ki bu durum geri çatma probleminin eksik belirtili olmasına neden olur. Önceki çalışmalar bu problemi aşmak için yinelemeli geri çatma yöntemleri önermiştir. Bu yöntemlerin en önemli zayıflığı, yüksek hesaplama maliyetidir. Bu sorun toplam değişinti (Total Variation: TV) en küçüklenmesini kullananarak, hesaplama açısından verimli filtrelenmiş geri projeksiyon (filtered backprojection: FBP) temelli yöntem ile ele alınmıştır. 2B modifiye Shepp-Logan fantomu önerilen methodun performans değerlendirmeleri için kullanılmıştır. Önerilen yöntemin üstünlüğü niceliksel ve niteliksel ölçütlerle gösterilmektedir. Tezin ikinci amacı, İstanbul Teknik Üniversitesi Makine Fakültesinde üretilen manyetik nanopartiküllerin (Magnetic Nanoparticles: MNPs) kontrast maddesi olarak kullanarak BT'nin kontrast duyarlılığını arttırılmasıdır. Agaroz jel içindeki beş farklı çekirdekli manyetik nanopartiküllerden kaynaklı piksel yoğunluğu artırımları analiz edilmiştir. Sonuçlar manyetik nanopartiküllerin BT için kontrast madde olarak kullanılabilirliğini doğrulamaktadır.

Anahtar kelimeler: seyrek BT, filtrelenmiş geri projeksiyon, toplam değişinti, manyetik nanopartüküller, kontrast artırımı.

Acknowledgements

I would like to express my deep gratitude to Professor Bülent YILMAZ and Associate Professor İsa YILDIRIM, my research supervisors, for their patient, guidance, encouragement and useful meetings during my master. We had many useful deliberations in my research work and they have always supported me with their academic knowledge and advices during this challenge. I would like to thank to Associate Professor İsa YILDIRIM for great and useful deliberations through this road even if we have studied in different cities and his belief in my potential. I cannot express my gratitude in words to my supervisors.

My grateful thanks are also extended to Professor Celaletdin ERGUN and his team who provided the magnetic nanoparticles used in my study.

I am also grateful to Grad Student Office in AGU. We shared our the saddest and the happiest moments along this journey. More importantly, I want to present my gratitude to my fellow travellers Mustafa Çağatay KOÇER and Rukiye Nur KAÇMAZ. I regard myself lucky to have been piece of these amazing graduate students.

Finally, I am so grateful to my family and my best friend Bengisu SOYKUVVET for their great support and endless love in my life. I couldn't have made my MSc without their great support.

Table of Contents

List of Figures

List of Tables

To my father

Chapter 1

Introduction

In this Chapter, problems of the subject will be briefly reviewed and the purpose, contributions, and outline of the thesis will be specified.

1.1 Problems

Cancer is a common disease among both men and women population and its mortality and morbidity rates are very high. Cancer occurs when the cells of the body start to increase their population unrestrainedly. According to American Cancer Society, it is estimated that there will be 1,735,350 new cancer patients and 609,640 deaths from cancer in 2018 in the U.S. As shown in Figure 1.1.1, cancer was remained the second cause of death from 1975 to 2015 years and became nearly the same with heart diseases which were top leading causes of death in the same period.

Cancer diagnosis and treatment process requires accurate imaging in order to determine the stage of cancer correctly as well as to determine the size and position of tumorous tissues. Advanced imaging modalities are used for detecting and monitoring of cancer and they have a major impact on the reduction of

mortality and morbidity rates of cancer. For instance, computed tomography (CT), digital mammography and tomosynthesis, magnetic resonance imaging (MRI), positron emission tomography (PET) and their integration with other modalities are widely performed in all steps of cancer management [1].

Stemming from the development of X-ray by Wilhelm C. Rontgen, advanced imaging techniques have been developed and enabled more efficient diagnostic modalities in the medical imaging field.

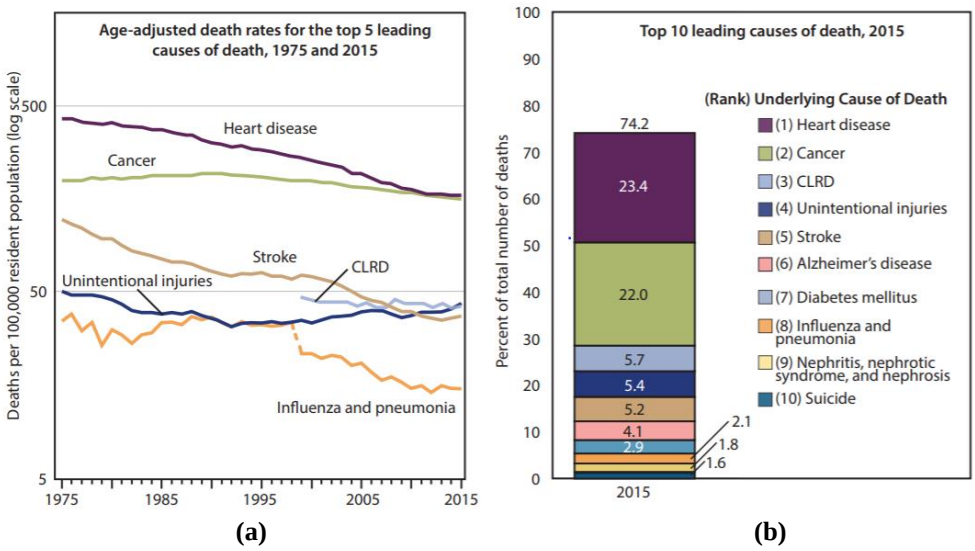

Figure 1.1.1 (a) Mortality causes in the U.S. in between 1975 and 2015 years, (b) percentage of top leading causes of mortality in 2015 in the U.S [2].

The most important one, CT, is a breakthrough for clinical imaging as well as industrial applications. CT is an imaging modality that provides two-dimensional (2D) slices of a three-dimensional object using the series of projections taken from different angles around the object. CT is able to provide accurate detailed images of body and picture even small abnormal tissue such as a tumor. Thus, CT is commonly used in many clinical applications such as diagnosing and monitoring treatment of cancer [3], examination of coronary artery diseases [4] and imaging trauma [5].

It is well known that the demand for installing CT imaging systems in hospitals has been increasing worldwide due to the clinical benefits of CT [3].

The statistics support that the scans of CT imaging expanded tremendously during the quarter of a century in the US as shown in Fig. 1.1.2. The corresponding figure indicates that there has been a rapid increase in CT scans, because of the CT is the most useful diagnostic development around the world when compared with other X-ray modalities such as projectional radiography [6].

Despite its superiority of imaging with short scanning and reconstruction time, the radiation dose still remains its main limitation. The quality of reconstructed image directly related to radiation dose [7]. In order to obtain acceptable quality images, the radiation dose have to be used at a certain value. However, it is well known that ionizing radiation can lead to harmful consequences in long-term exposure. The former studies indicated that ionizing radiation brings about DNA modifications and these permanent changes depend on the complexity of diversity on DNA [8].

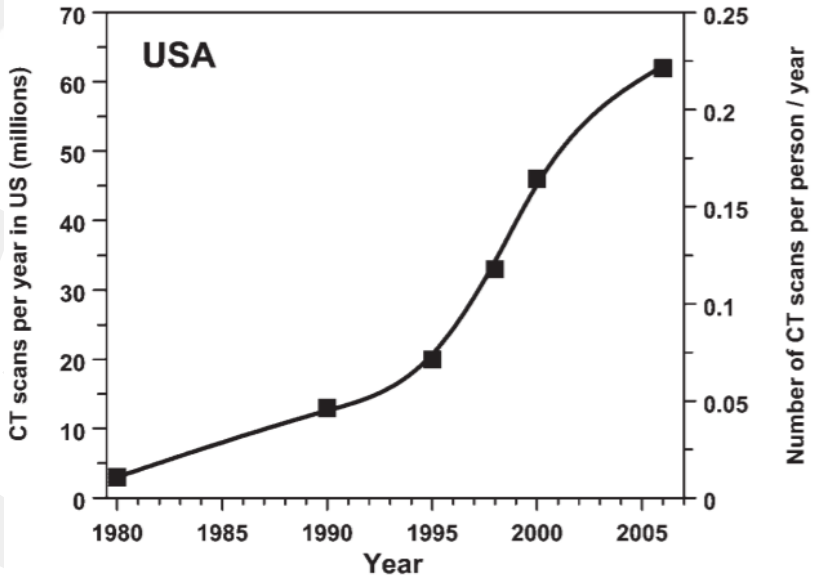

Figure 1.1.2. Trend in a number of CT scans per year in the US with the number of scans per person per year [9].

Although CT imaging is ubiquitous for clinical diagnosis, the adverse outcomes of X-ray are debatable issues [9]. In order to determine the level of radiation dose, there are several measures, for instance, absorbed dose and effective dose. The measurement of absorbed dose is gray (Gy) that equals to the

energy per unit mass (1 Gy= J/kg). The commonly used effective dose is referred for sieverts (Sv) for non-uniform exposures [6]. The measurements are significant to compare safety level of radiation received from CT with natural background radiation [10]. As though, the radiation of CT is at a safe level as comparable as natural radiation, overuse of CT can lead significant issues on human's health. Inherently, CT uses high radiation dose when compared with other X-ray imaging modalities as shown in Figure 1.1.3 [6]. The individual examination can be associated with small radiation but when taken into account the yearly scans it becomes a significant number. The prediction of the relation between cancer risks and radiation is coming from studies that were done with people who were exposed to atomic bombs in Nagasaki and Hiroshima [11].

Study Type	Relevant Organ	Relevant Organ Dose* (mGy or mSv)
Dental radiography	Brain	0.005
Posterior–anterior chest radiography	Lung	0.01
Lateral chest radiography	Lung	0.15
Screening mammography	Breast	3
Adult abdominal CT	Stomach	10
Barium enema	Colon	15
Neonatal abdominal CT	Stomach	20

Figure 1.1.3. Different X-ray imaging modalities and their relevant organ doses [6].

In the research field, there exists several reports that indicate the radiation can be associated with cancer risks. At the beginning of the eighties, Doll and Peto indicated that 0.5% mortality from cancer in the US was depended on diagnostic X-ray back then [12]. Gonzalez et al., 2004 showed that in the UK approximately 0.6% of the cumulative risk of cancer, the percentage equals to about 700 people annually, to age 75 years can be assignable to medical diagnostic X-rays [11]. Brenner et al., 2007 states that between 1991 and 1996, approximately 0.4% of all cancers in the US can be due to radiation of CT

researches [6]. The cancer risk comes from diagnostic X-rays differs according to the frequency of exposure annually.

In order to lower the annual number of cancer cases originating from X-ray, either the radiation dose in an examination should be decreased to agreeable level or frequency of examinations should be reduced [11]. This principle is called 'As Low As Reasonably Achievable' (ALARA) that aims radiation protection for human health in medical imaging [9].

In CT imaging, there is a trade-off between image quality and radiation dose. Thus, developing the new strategies for reducing radiation dose without compromising image quality is a hot topic in the research field. Using advanced reconstruction algorithms can provide acceptable CT imaging quality from low dose scans. In order to realize this, there exists numerous studies proposed to estimate target image from insufficient projection data by limiting the number of projections without lowering the reconstruction quality [13], [14].

It is well known that CT is able to visualize hard tissues surrounding by soft tissues successfully due to existing of natural contrast between hard and soft tissues [15]. However, it is difficult to distinguish accurately different soft tissues which have similar CT numbers [16]. Therefore, researchers have studied to overcome this issue. In order to increase the sensitivity of CT imaging, contrast agents have been developed. According to IMV U.S. Medical Information Division survey, in 2010 55% of the total CT scans performed with using contrast agents to improve the sensitivity of imaging results in the U.S. Because of usage restrictions for traditional contrast agents, researchers have directed to nanotechnology because of unique properties of nanoparticles. Consequently, using nanoparticles as the contrast agent is a phenomenon for both clinical and research areas.

1.2 Aims and Contributions of Thesis

This thesis is motivated by desires to improve low dose CT imaging reconstruction results and to increase the sensitivity of CT imaging. In order to realize the first aim, one of the traditional reconstruction-based methods is developed and its efficiency is investigated using analytical phantom. The second aim which is the improving sensitivity of CT imaging is executed with under experimental protocol and analyzing of the results. Both studies show promising outcomes for CT imaging.

The thesis contributions can be arranged in two main categories:

1. Development of new computationally efficient reconstruction method using traditional and compressed-sensing based methods for low dose CT imaging
2. Investigating feasibility of the magnetic nanoparticles as contrast agents for CT imaging

1.3 Outline of Thesis

Chapter 2 contains fundamentals of X-ray imaging and brief information of CT, medical background of CT imaging and existing CT reconstruction methods which are very popular in CT such as filtered backprojection (FBP), algebraic reconstruction technique (ART) and compressed sensing-based method total variation (TV) are explained.

Chapter 3 includes related work and relevant CT reconstruction methods and proposes a new approach that performs low CT image reconstruction

iteratively in an efficient way and the simulation results are provided in this Chapter.

Chapter 4 consists of background about nanosized contrast agents in CT imaging and investigating the usage of novel magnetic nanoparticles as contrast agents for CT imaging.

Finally, the contributions of the thesis are discussed and future work of the thesis is given in Chapter 5.

Chapter 2

Background

This Chapter reviews the X-ray imaging, the mathematical basis of CT imaging and fundamental reconstruction techniques to demonstrate the capabilities of various techniques and challenges. The detailed theory of two dimensional (2D) CT reconstruction is well known. Thus, brief information about underlying mathematics of CT will be given and with the extension of some main reconstruction methods that will provide base for the proposed method.

2.1 X-ray Imaging

This Section reviews the X-ray imaging in terms of X-ray generation, interactions of X-ray with matter and brief information about CT scanner. These are not our focuses to give all detailed information about X-ray and CT, and the reader is directed to Buzug (2008) for a more detailed explanation.

2.1.1. X-ray Generation

As is mentioned in Chapter 1, CT uses attenuated X-rays that are acquired around the object at different angles to reconstruct 2D images or 3D volumes of structures. X-ray radiation was discovered accidentally by Wilhelm Röntgen in 1895 and he received the Nobel Prize due to this invention. After this invention, the foundations of diagnostic medicine have been devised however production of X-rays has almost stayed the same. X-ray imaging modalities use vacuum tube to produce X-rays and the illustration of the typical X-ray tube is given in Figure 2.1.1.1.

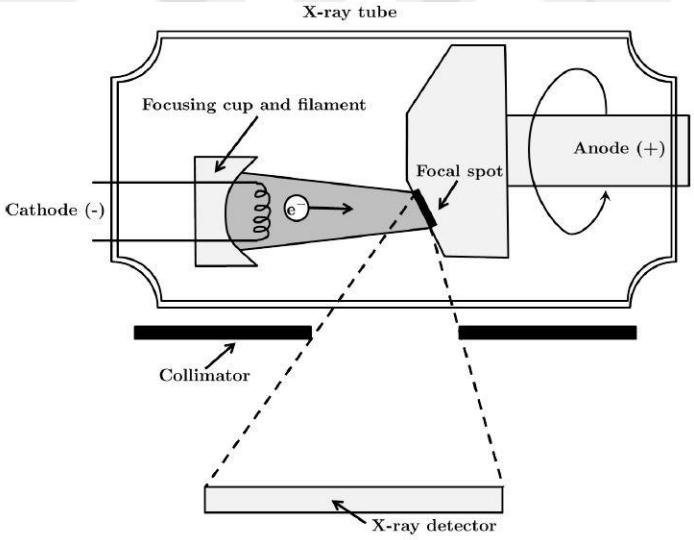

Figure 2.1.1.1 A typical X-ray tube. The basic components of typical X-ray tube are anode and cathode. The cathode provides the electrons and anode supplies the target material. When the cathode filament is heated to specified energy, the electrons are accelerated from cathode to anode in the electric field [17].

The acceleration voltage is chosen in a range between 25kV and 150kV for medical diagnostics [18]. Since the temperature at the focal point can reach 2600-2700°C, the anode is rotated at a very high speed in order to avoid melting of the target. The heat and X-ray radiation are produced by bombarding the target with high-speed accelerated electrons. Over 99% of input energy is converted into heat and only approximately 1% of the energy turns into X-ray photons [19]. The X-

ray photons are detected by X-ray detector and intensity of X-ray radiation depends on the type of target material and the number of electrons hit the target. The potential difference between the cathode and anode effects the energy level of X-ray photons.

The electron scattering continues until electrons approximately stay immobile that means loses all own energy. All X-ray photons provided from the bombardment of target atoms create continues X-ray spectrum. If the electron interacts with the target atom and loses all energy acutely, initial kinetic energy equals to a maximum energy of X-ray photon (minimum wavelength $\lambda_{\min}$):

$$\frac{1}{2}\left(m_e v_e\right)^2 = \frac{hc}{\lambda_{\min}}. \qquad \textbf{(2.1.1.1)}$$

As is seen in Figure 2.1.1.2, the peaks of spectrum correspond to characteristic radiation. If the electrons have sufficient energy, an electron is ejected from K shell of target material and peaks are labeled as K_α and K_β which have high intensities [17]. Moreover, because of self-absorption, the intensity reduces with the increased anode angle (β) [18]. Low energy X-rays which have long wavelength are absorbed more strongly by matter. In practice, suppressing low energy X-ray photons is necessary because they increase the total radiation exposure and produce artifacts in reconstructed images [18]. This process is called beam filtering in practice.

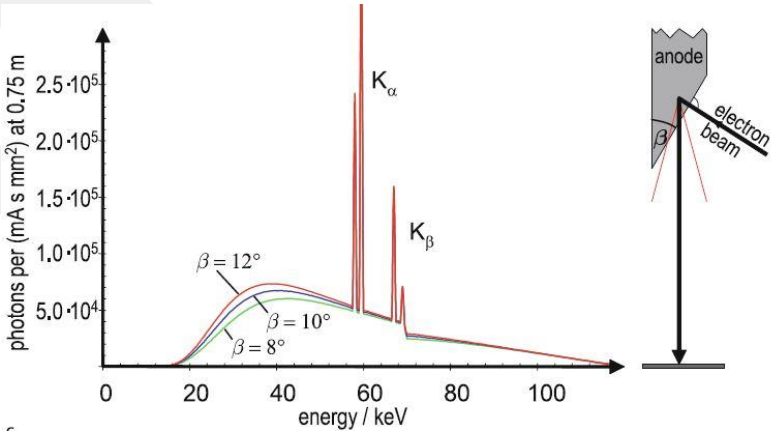

Figure 2.1.1.2 X-ray spectrum of a tungsten anode illustration for different anode angles. The spectrum illustrates the continuous radiations at different energy levels and the peaks K_α and K_β represent the characteristic radiation [18] simulated at 120 kV.

2.1.2. Interaction of X-ray with Matter

When X-ray photons passing through the matter, they lose their energy because of absorption and scattering interactions between X-ray beams and matter. The underlying principle of X-ray imaging is that the determination of how much X-ray photons are attenuated when they pass through the object. X-ray attenuation is based on Beer-Lambert law as given below:

$$I(x) = I_0 \exp(-\sum_i \mu_i x_i), \qquad \textbf{(2.1.2.1)}$$

where, I_0, $I(x)$ are X-ray intensities before and after the matter and μ_i, x_i are attenuation coefficients and dimensions of volumes along the X-ray beam. The calculation of attenuation of X-ray photons by the matter can be modeled by discrete attenuation coefficients in Figure 2.1.2.1.

To reconstruct the internal structure of an object, the measured attenuation coefficients that are converted to Hounsfield unit (HU) scale. The HU values of distilled water, air and bone are 0, -1000 and 1000 HU, respectively. The transformation formula as follows:

$$HU = \left(\frac{(\mu_{tissue} - \mu_{water})}{\mu_{water}} \right) \times 1000. \qquad \textbf{(2.1.2.2)}$$

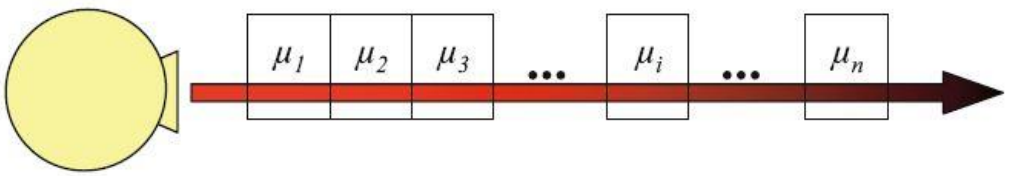

Figure 2.1.2.1 Attenuation of X-ray beam while passing through the matter which includes various attenuation coefficients [18].

2.1.3. Computed Tomography

As discussed earlier, computed tomography is an irreplaceable imaging technique in clinical applications due to its superior features. It visualizes the images of internal structures of an object noninvasively. There has been a numerous number of texts explaining the history, principles, and advances of CT such as Webb (1990) that explains the classical tomography in details, Buzug (2008) and Hsieh (2009) give broad information about underlying mathematics and advances of CT. In this Section, we will focus on the fundamental knowledge of CT imaging to a certain extent.

When a chest X-ray is taken into account (given in Figure 2.1.3.1), only certain anatomical structures are observed. The bone structures appear lighter than soft tissues because they attenuate X-rays more strongly. Moreover, lungs seem as the darkest regions in the radiograph due to less attenuation of X-ray beams by air. However, the final 2D image is the result of the 2D projection of a 3D structure. Thus, a final image obtained from many planes whereas the planes superimposed on each other and this leads to loss of depth information [20]. Other problems with conventional radiography that it is not adequate in the way of the visualization and differentiation of soft tissues. It is insufficient to spatially resolving soft tissue structures such as blood and lesion details [21].

Figure 2.1.3.1 The X-ray radiograph of chest [21].

CT is a sectional imaging technique offers superior results. Unlike the conventional X-ray radiography, CT acquires projections from different angles in

specified planar slice and reconstruct the 2D images from these measurements. This solves the plane overlapping problem and CT slice thickness is generally a few millimeters and resulting images show the body structures in a cross-sectional manner with lower than 1mm spatial resolution [21]. Despite there is a number of different CT imaging designs, present thesis confines in classical parallel-beam CT scanner which is sketched in Figure 2.1.3.3. As can be seen in Figure 2.1.3.3, the X-ray source generates parallel X-ray beams and parallel projections are measured by detector simultaneously. After one scan, the gantry is rotated to its new position and projection data is gathered at this angle.

Later advance models have been developed to reduce the motion artifacts and the scan time which leads to decreasing the time of data acquisition in early designs of CT imaging systems. In order to reach improved image quality, the number of beams was increased. Moreover, the cover angle of beams and detector arrays were extended to record more measurements at each pulse of the X-ray tube [19]. A more detailed description of generations of CT scanner can be found in Hsieh (2009) and Webb (2006).

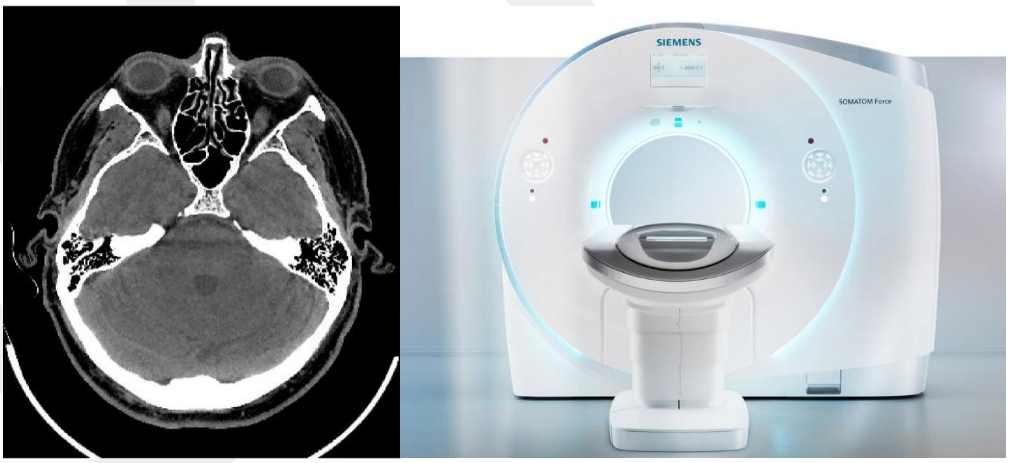

(a) **(b)**

Figure 2.1.3.2 (a) The CT head image acquired with the GE LightSpeed VCT 2005 [19] and (b) Siemens SOMATOM Force CT imaging system [22].

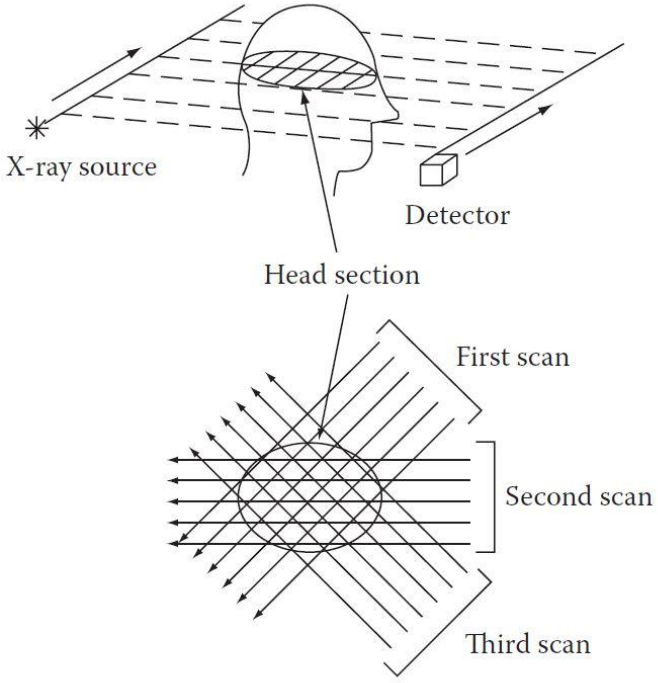

Figure 2.1.3.3 The demonstration of parallel-beam tomography scan. The X-ray flux passes through the object and the detector is located opposite side to generate projections at different angles. This procedure continues at many angles until sufficient set of projection data is obtained [21].

2.2 Mathematical Basis of CT

In this Section, the fundamental terminologies used in present thesis will be defined. Firstly, the projections will be explained with Radon transformation that is the key component of CT image reconstruction. The most common image reconstruction techniques will be surveyed an extension of one of the analytical reconstruction technique filtered backprojection and it will be the base for the new reconstruction algorithm.

2.2.1. Radon Transformation

On 30 April 1917, Austrian mathematician Johann Radon introduced a mathematical model as a solution for the inverse problem in CT imaging titled as 'On the Determination of Functions from their Integrals along Certain Manifolds' [23]. It is a building block of CT image reconstruction and ensuing studies have emerged from Radon transformation. In 2D parallel-beam geometry, the image is reconstructed from a set of line integrals that are acquired from parallel aligned beams at different angles. From now on this thesis, $f(x, y)$ represents the two-dimensional image to be reconstructed.

Figure 2.2.1.1 illustrates the parallel projection lines passing through the tissue at a certain projection angle θ of the X-ray tube and the detector, respectively. The spatial distribution of density values of tissue to be reconstructed are discrete values yet we assume continues.

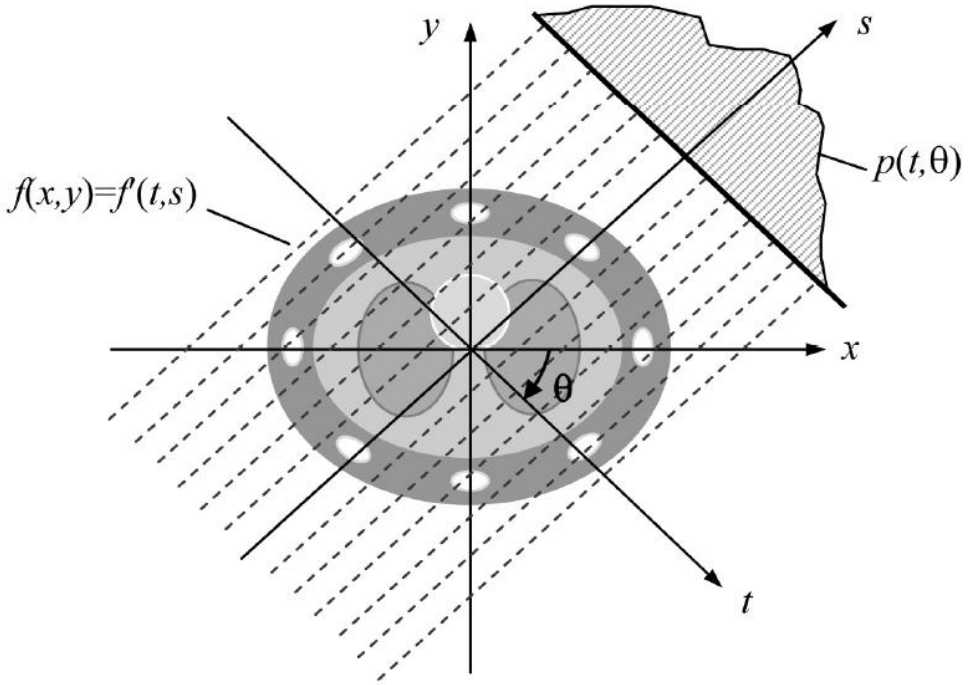

Figure 2.2.1.1 Illustration of Radon transform in parallel-beam geometry on original and rotated coordinate systems [19].

The X-ray intensity values before and after object are I_0 and I respectively and attenuation is calculated by Beer-Lambert law as given before. We suppose that X-ray beam attenuated by the object through the line L. In order to obtain line integral value of the object function formulated as follows:

$$\int_L f(x,y)dl = -\ln\frac{I}{I_0}. \qquad \textbf{(2.2.1.1)}$$

As can be seen in Figure 2.2.1.1, at an angle θ the projection value can be written as:

$$p(t,\theta) = \int_{-\infty}^{\infty}\int_{-\infty}^{\infty}(f(x,y)\delta(x\cos(\theta)+y\sin(\theta)-t)dxdy\,. \qquad \textbf{(2.2.1.2)}$$

The relation of original patient coordinate (x,y) and rotating coordinate (t,s) systems are given as follows:

$$t = \left(x\cos(\theta)+y\sin(\theta)\right) \qquad \textbf{(2.2.1.3)}$$

and

$$s = \left(-x\sin(\theta)+y\sin(\theta)\right). \qquad \textbf{(2.2.1.4)}$$

Collected projection data (line integrals) over the angular range (π) used to reconstruct the tomographic image and the data are regularized in a two-dimensional map which is called sinogram [24]. All projections are assembled vertically in this way and a single projection corresponds to a vertical line in the sinogram. The illustration of sinogram formation is given in Figure 2.2.1.2.

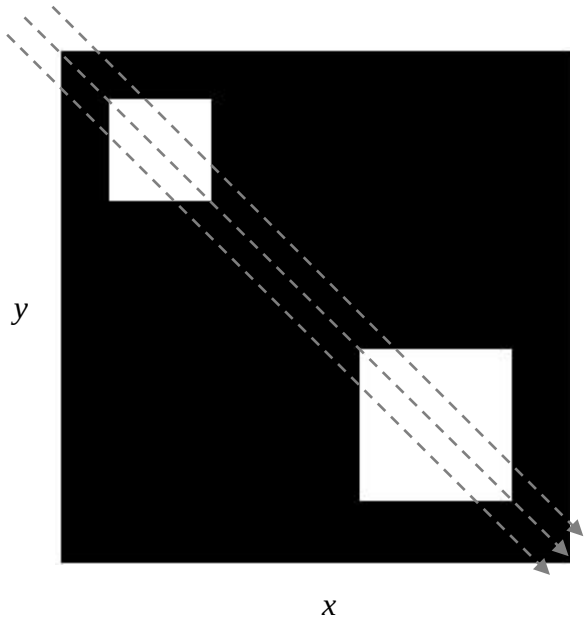

(a)

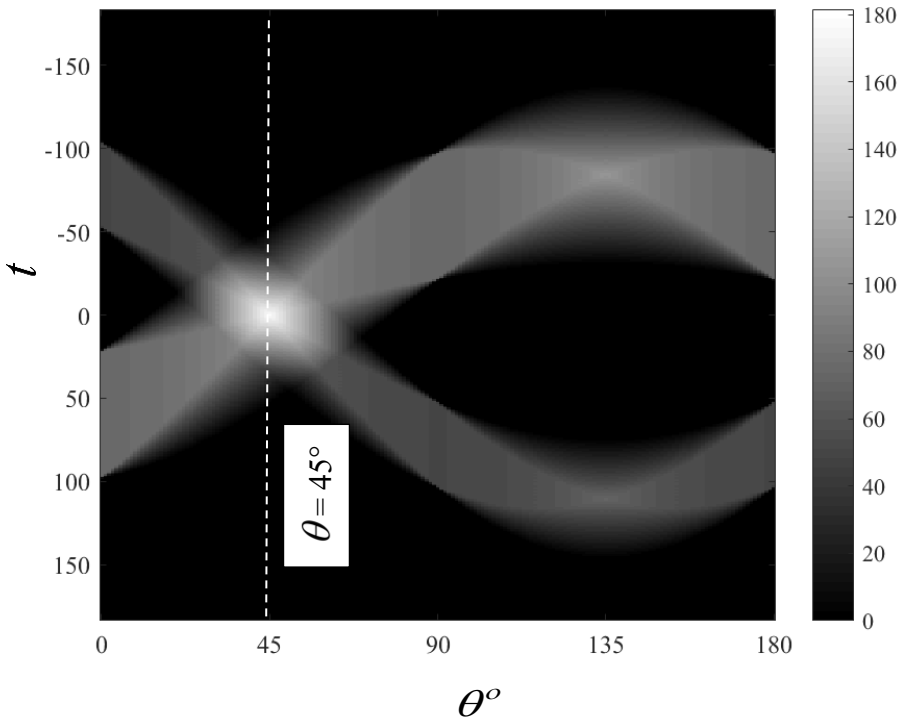

(b)

Figure 2.2.1.2 (a) The 256× 256 pixel image was generated in MATLAB. (b) The sinogram of image simulated using Radon transformation.

2.2.2. Fourier Slice Theorem

Fourier Slice Theorem is the major component of CT image reconstruction and the theorem related to the understanding of the mathematical basis of tomographic imaging [25]. The theorem states that one-dimensional (1D) Fourier transform (FT) of each projection ($p_\theta(t,\theta)$) with respect to the radial line equals to the 2D FT of the image $(F(u,v))$ at θ. Ultimately, inverse 2D FT can be calculated from 1D FT of the projections to recover the original image ($f(x,y)$) as shown in Figure 2.2.1.3. Each projection gives the access of a slice at a certain angle in the frequency domain to recover the image accurately. The main steps of Fourier Slice theorem are given as below:

1) Calculation of 1D FT of each projection respect to a radial line
   $P_\theta(q) \longleftarrow p_\theta(t)$
2) Construction of 2D Fourier representation of the image from 1D FT of projections
   $F(u,v) \longleftarrow P_\theta(q)$
3) Calculation of inverse FT to acquire the image function
   $f(x,y) \longleftarrow F(u,v)$

The mathematical notation of Fourier slice theorem is denoted as follows:

$$P_\theta(q) = \int_{-\infty}^{\infty} p_\theta(t) e^{-i2\pi qt} dt \,, \qquad \textbf{(2.2.2.1)}$$

$$F(u,v) = \int_{-\infty}^{\infty}\int_{-\infty}^{\infty} f(x,y) e^{-i2\pi(ux+vy)} dxdy \,, \qquad \textbf{(2.2.2.2)}$$

$$P_\theta(q) = F(q\cos(\theta), q\sin(\theta)) \,, \ \forall q \in \mathbb{R}, \forall \theta \in \mathbb{R}. \qquad \textbf{(2.2.2.3)}$$

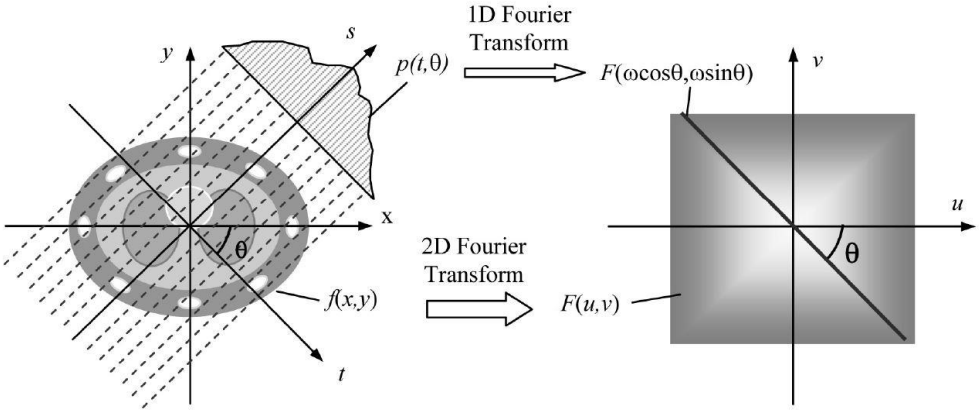

(a)

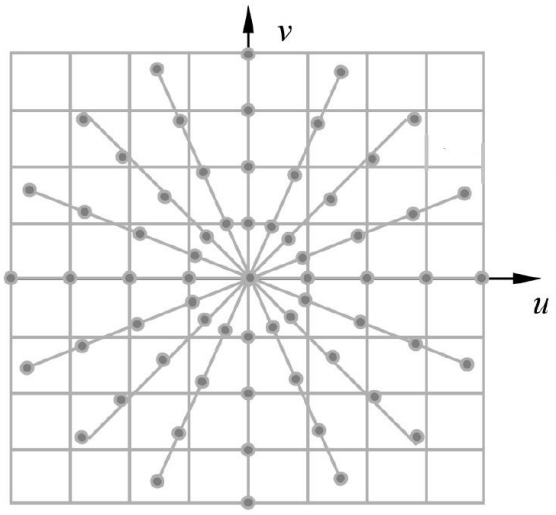

(b)

Figure 2.2.2.1 (a) The demonstration of Fourier slice theorem and (b) sampling pattern in Fourier space [19].

2.2.3. Simple Backprojection

The Radon transform takes the forward projection of a 2D image ($f(x, y)$) and places the data into sinogram. In order to recover the 2D object from its projections, every projection profile is smeared back into spatial space through the direction of the corresponding ray. This procedure is named ‘backprojection’

[26]. It is essential for image reconstruction. This process can be formulated by the following:

$$f(x,y) = \int_0^{\pi} p_\theta(t)d\theta = \int_0^{\pi} p_\theta(x\cos(\theta) + y\sin(\theta))d\theta\,. \qquad \textbf{(2.2.3.1)}$$

Unfortunately, the process does not recover the desired object instead generates a blurred version of the image. Because of non-negativity of projection data, the simple back-projection assigns positive values to the entire 2D image even to pixels of outside the object [18]. The example of simple backprojection is given in Figure 2.2.3.1. As can be seen from the figure, the backprojection produces a blurred result while a high number of projections are used.

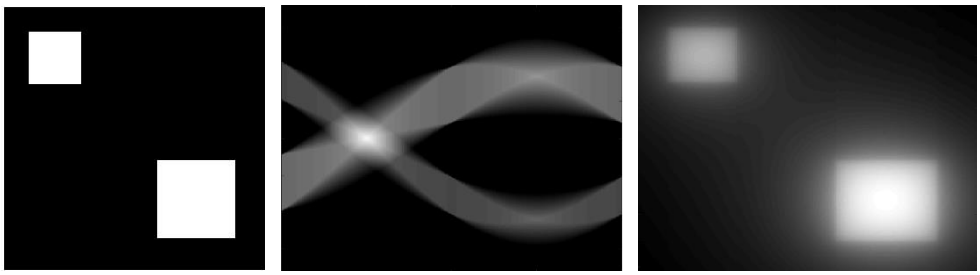

(a) **(b)** **(c)**

Figure 2.2.3.1 The example of backprojection process: (a) The 256×256 synthetic image, (b) the sinogram of the image, (c) the simple backprojection of the image using 180 projections.

2.2.4. Siddon's Algorithm

Defining an exact radiological path for CT image reconstruction is necessary. The reason behind this is to determine the intersection of the ray with voxels when the X-ray beam passes through the object. In view of the complexity of CT geometry and a great number of CT data, the determination of weighting parameters as well as voxel indices are time-consuming and difficult. In order to overcome these problems, Siddon presented an efficient algorithm to determine the exact radiological path for 3D CT array in 1985 [27]. The algorithm is commonly preferred in calculating the ray path of 2D and 3D image

reconstruction for different studies in medical imaging. Figure 2.2.4.1 illustrates the intersection of the ray and a 2D image. In this case, the pixels are considered as the intersection regions of orthogonal sets of equally spaced, parallel lines. When the corresponding figure is considered, the ray can be represented parametrically as follows:

$$\begin{aligned} X(\alpha) &= X_1 + \alpha(X_2 - X_1), \\ Y(\alpha) &= Y_1 + \alpha(Y_2 - Y_1), \end{aligned} \qquad \alpha \in [0,1] \qquad \textbf{(2.2.4.1)}$$

where, 1 and 2 points entry and exit points of the ray respectively.

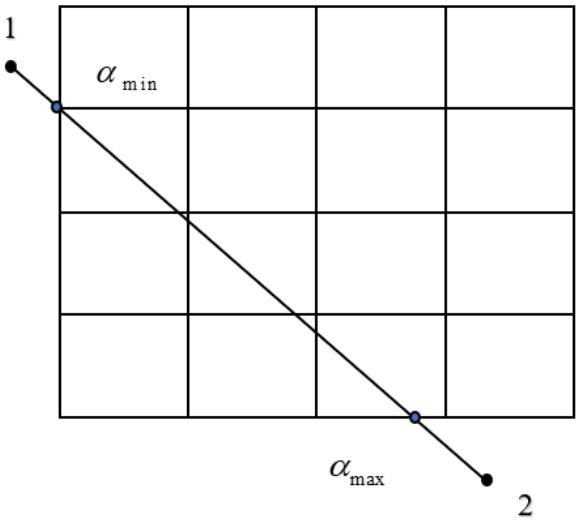

Figure 2.2.4.1 The entry and exit points of the ray are $\alpha = \alpha_{min}$ and $\alpha = \alpha_{max}$ respectively.

For a 2D CT array of $(N_x - 1, N_y - 1)$ voxels, the orthogonal sets of equally spaced, parallel planes can be denoted as:

$$X_{plane}(i) = X_{plane}(1) + (i-1)dx \qquad (i = 1,...,N_x), \qquad \textbf{(2.2.4.2)}$$

$$Y_{plane}(j) = Y_{plane}(1) + (j-1)dy \qquad (\mathrm{j} = 1,...,N_y),$$

where d_x and d_y represent the distances between x, y planes. Moreover, these distances exhibit the lengths of sides of pixels. The intersection of the ray with the sides of array results in the parametric values $\alpha_{\min}$ and $\alpha_{\max}$. The formulations of parametric values as given followings:

$$If\,(\mathrm{X}_2 - X_1) \neq 0,$$

$$\alpha_x(1) = \frac{[\mathrm{X}_{plane}(1) - \mathrm{X}_1]}{(\mathrm{X}_2 - X_1)}, \qquad \alpha_x(N_x) = \frac{[\mathrm{X}_{plane}(N_x) - X_1]}{(\mathrm{X}_2 - X_1)}, \tag{2.2.4.3}$$

for $\alpha_y(1), \alpha_y(N_y)$ similar formulations are written. In $(\mathrm{X}_2 - X_1) = 0$ case, the ray is perpendicular to x axis and denominator of equation (2.2.4.3) will be zero. If α_x and α_y values undefined, these values can be excluded from all following expressions. The formulation of $\alpha_{\min}$ and $\alpha_{\max}$ values are given as:

$$\alpha_{\min} = \max\left\{0, \min\left[\alpha_x(1), \alpha_x(N_x)\right], \min\left[\alpha_y(1), \alpha_y(N_y)\right], \right\},$$

$$\alpha_{\max} = \min\left\{0, \max\left[\alpha_x(1), \alpha_x(N_x)\right], \max\left[\alpha_y(1), \alpha_y(N_y)\right] \right\}, \tag{2.2.4.4}$$

where min and max functions choose the minimum and maximum values respectively from their arguments. Only certain intersected planes have these parametric values in this range ($\alpha_{\min}$ and $\alpha_{\max}$). The specified range of indices are given below:

$$If\,(\mathrm{X}_2 - X_1) \geq 0,$$

$$i_{\min} = N_x - \frac{\left[X_{plane}(N_x) - \alpha_{\min}(\mathrm{X}_2 - X_1) - X_1\right]}{dx}$$

$$i_{\max} = 1 + \frac{\left\lfloor X_1 + \alpha_{\max}(\mathrm{X}_2 - X_1) - X_{plane}(1) \right\rfloor}{dx}.$$

$$If\ (\mathrm{X}_2 - X_1) \le 0, \qquad \textbf{(2.2.4.5)}$$

$$i_{\min} = N_x - \frac{\left\lfloor X_{plane}(N_x) - \alpha_{\max}(\mathrm{X}_2 - X_1) - X_1 \right\rfloor}{dx},$$

$$i_{\max} = 1 + \frac{\left\lfloor X_1 + \alpha_{\min}(\mathrm{X}_2 - X_1) - X_{plane}(1) \right\rfloor}{dx},$$

which are similar formulations for other indices ($j_{\min,}\, j_{\max}$). The range of indices ($i_{\min,} i_{\max,} j_{\min,}\, j_{\max}$) and their corresponding parametric values that indicate the intersections as follows:

$$If\ (\mathrm{X}_2 - X_1) > 0,$$

$$\{\alpha_x\} = \{\alpha_x(i_{\min}), ..., \alpha_x(i_{\max})\}.$$

$$If\ (\mathrm{X}_2 - X_1) < 0, \qquad \textbf{(2.2.4.6)}$$

$$\{\alpha_x\} = \{\alpha_x(i_{\max}), ..., \alpha_x(i_{\min})\}.$$

where $\alpha_x(i) = \frac{\left\lfloor X_{plane}(i) - X_1 \right\rfloor}{(\mathrm{X}_2 - X_1)} = \alpha_x(i-1) + \left\lfloor \frac{dx}{(\mathrm{X}_2 - X_1)} \right\rfloor$, using similar expressions for $\{\alpha_y\}$.

Then, the calculated α_x and α_y values are sorted in the range $\alpha_{\min}$ and $\alpha_{\max}$. If $\alpha_{\max}$ equals or less than $\alpha_{\min}$, then the ray does not intersect with the array.

$$\{\alpha\} = \{\alpha_{\min}, merge[\{\alpha_x\}, \{\alpha_y\}], \alpha_{\max}\}, \qquad \textbf{(2.2.4.7)}$$

where the last term has the index represents with n as follow:

$$n = (i_{\max} - i_{\min} + 1) + (j_{\max -} j_{\min} + 1) + 1. \qquad \textbf{(2.2.4.8)}$$

The length of pixel intersection $l(m)$ is given below for two intersections m and $m-1$:

$$l(m) = \mathrm{d}_{12}\left[\alpha(m) - a(m-1)\right], \qquad (m = 1, ..., n) \qquad \textbf{(2.2.4.9)}$$

$$d_{12} = \left[(X_2 - X_1)^2 + (\mathrm{Y}_2 - Y_1)^2\right]^{1/2}. \qquad \textbf{(2.2.4.10)}$$

The pixel $\left[i(m), j(m)\right]$ corresponds to the intersection of m and $m-1$ that contains midpoint of the intersections. The mathematical formulations of indices are given as:

$$i(m) = 1 + \left[X_1 + \alpha_{mid}(X_2 - X_1) - X_{plane}(1)\right] / d_x,$$

$$\mathrm{j}(m) = 1 + \left[Y_1 + \alpha_{mid}(\mathrm{Y}_2 - Y_1) - Y_{plane}(1)\right] / d_y, \qquad \textbf{(2.2.4.11)}$$

where α_{mid} is formulated by following:

$$a_{mid} = \frac{\left[\alpha(m) + \alpha(m-1)\right]}{2}. \qquad \textbf{(2.2.4.12)}$$

Finally, the radiological path d can be written as the following formulation,

$$d = \sum_{m=1}^{m=n} l(m)\rho\left[i(m), j(m)\right] = d_{12}\sum_{m=1}^{m=n}\left[\alpha(m) - \alpha(m-1)\right]\rho\left[i(m), j(m)\right]. \qquad \textbf{(2.2.4.13)}$$

2.3 Reconstruction Methods of CT

There exists numerous studies proposed to estimate target image from the projection data. In order to reconstruct the image from the projections, the reconstruction methods proposed in the literature can be divided into two major

groups as analytical methods and iterative methods [28]. In this section, we will concentrate on algebraic reconstruction technique (ART) and filtered backprojection (FBP) in particular.

2.3.1. Filtered Backprojection (FBP)

The most commonly used analytical method for CT image reconstruction is filtered backprojection (FBP). When the computation time is one of main constraint, the Fourier transform based methods are widely preferred. Thus, FBP has a practical application in standard imaging modalities due to short reconstruction time [29]. There is a strong relation between FBP and Fourier Slice Theorem which was discussed in the former Section. In order to explain the idea behind FBP, Fourier Slice Theorem should be focused. The 1D FT of every projection data gives the value of object's 2D FT along the specified line. Then, mapping sufficient number of projection data into the Fourier space can construct 2D transform of the object and its simple inversion of Fourier results in a reconstruction.

As its name refer, FBP consist of two major components as filtering and backprojection. Firstly, the filtering step works out for the rescaling of each projection in the frequency domain. Secondly, the backprojection step is necessary to smear out every filtered projection data into the spatial domain. Although filtered backprojection has been used in practice commonly, there are some limitations. The method usually assumes continues projections, unlike real algorithms, work on discrete data and it requires complete sampling in both angular and radial coordinates [26]**.** Image quality is also another problem. It cannot overcome striking artifacts also cannot hold missing data problems [18].

Firstly, the theory of FBP is presented and derived from Kak and Slaney (1988) and Hsieh (2009). Taking inverse Fourier transform of a 2D representation of an object, the function of the object can be written as:

$$f(x,y) = \int_{-\infty}^{\infty}\int_{-\infty}^{\infty} F(u,v)e^{j2\pi(ux+vy)}dudv\,. \qquad \textbf{(2.3.1.1)}$$

Cartesian coordinate system (u,v) is expressed in the polar coordinate system (q,θ) to define $F(u,v)$ in natural form because each FT of projection data is located in the polar coordinate system. The substitution can be done as follows,

$$\begin{aligned} u &= q\cos(\theta) \\ v &= q\sin(\theta) \end{aligned}, \qquad \textbf{(2.3.1.2)}$$

and

$$dudv = qdqd\theta\,. \qquad \textbf{(2.3.1.3)}$$

Then the inverse FT of object function in polar coordinate can be written as,

$$f(x,y) = \int_0^{2\pi}\int_{-\infty}^{\infty} F(q,\theta)e^{j2\pi q(x\cos\theta + y\sin\theta)}qdqd\theta\,. \qquad \textbf{(2.3.1.4)}$$

The equation (2.3.1.4) can be divided into two by summing θ from 0° to 180° and 180° to 360° as given below,

$$\begin{aligned} f(x,y) &= \int_0^{\pi}\int_0^{\infty} F(q,\theta)e^{j2\pi q(x\cos\theta + y\sin\theta)}qdqd\theta \\ &+ \int_0^{\pi}\int_0^{\infty} F(q,\theta+180°)e^{j2\pi q(x\cos(\theta+180°)+y\sin(\theta+180°))}qdqd\theta \end{aligned} \qquad \textbf{(2.3.1.5)}$$

In parallel sampling geometry, the formulation can be substituted with following using the symmetry property:

$$F(q,\theta+\pi) = F(-q,\theta). \qquad \textbf{(2.3.1.6)}$$

Using (2.3.1.5) and (2.3.1.6) equations, the relationship can be rewritten as:

$$f(x,y)=\int_0^{\pi}\left[\int_{-\infty}^{\infty}F(q,\theta)|q|e^{j2\pi qt}dq\right]d\theta, \qquad \textbf{(2.3.1.7)}$$

where t simplified by:

$$t=x\cos\theta+y\sin\theta\,. \qquad \textbf{(2.3.1.8)}$$

Using Fourier Slice Theorem indicated with equation (2.2.2.3), we can substitute $F(q,\theta)$ with $P(q,\theta)$ and construct the following formulation:

$$f(x,y)=\int_0^{\pi}\left[\int_{-\infty}^{\infty}\mathrm{P}(q,\theta)|q|e^{j2\pi qt}dq\right]d\theta \qquad \textbf{(2.3.1.9)}$$

and

$$S_\theta(t)=\left[\int_{-\infty}^{\infty}\mathrm{P}_\theta(q)|q|e^{j2\pi qt}dq\right]. \qquad \textbf{(2.3.1.10)}$$

The equation (2.3.1.10) illustrates the filtering operation, $S_\theta(t)$ is named modified or filtered projection. The filtered projections from different angles are summed to estimate spatial density distribution ($f(x,y)$) of a 2D image.

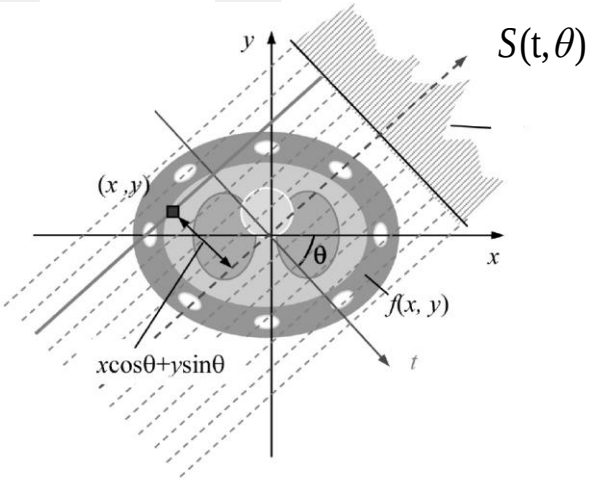

Figure 2.3.1.1 The demonstration of backprojection process in FBP reconstruction [19].

As can be seen in Figure 2.3.1.1, $x\cos\theta+y\sin\theta$ represents the distance from the point (x,y) to the line that passes through the center of coordinate

system. FBP states that the estimated image $f(x,y)$ at the location (x,y) is the summation of every filtered projection data that pass through the same point. The mathematical formulation is given below,

$$f(x,y)=\int_0^{\pi} S(x\cos\theta, y\sin\theta)d\theta\,. \qquad \textbf{(2.3.1.11)}$$

The FBP reconstruction is performed by summing FT of every projection data until whole frequency space is filled. Consequently, center regions are over enhanced and high-frequency regions are less present. In order to overcome this problem, every projection can be multiplied by weighting function that has a lower density in the center region and higher density at the high-frequency region.

The main steps of FBP reconstruction are given as follows:

1) For every projection angle θ, calculation of FT of the projection:
   $\mathrm{S}(\mathrm{t},\theta) \longrightarrow P(\mathrm{q},\theta)$
2) Multiply each $P(\mathrm{q},\theta)$ with weighting function (high-pass filtering) and inverse FT:
   $|q|\,P(\mathrm{q},\theta) \longrightarrow \mathrm{S}(\mathrm{t},\theta)$
3) Backprojection of modified projection data:
   $S(x\cos\theta, y\sin\theta) \longrightarrow f(x,y)$

Practical implementation of FBP reconstruction differs from the theory. Because of real data are discrete and spatially limited, projections are band-limited in the range between $-w$ and w. The assumption can be written as:

$$S(t,\theta)=\int_{-w}^{w} P(\mathrm{q},\theta)|q|e^{j2\pi qt}dq\,. \qquad \textbf{(2.3.1.12)}$$

To avoid aliasing, the bandwidth should satisfy Nyquist criteria:

$$w = \frac{1}{2\tau} \text{ cycles/mm.} \qquad \textbf{(2.3.1.13)}$$

The original ramp filter $|q|$ can be multiplied by a window function in frequency domain.

$$H(q) = |q| \mathrm{W}(q), \qquad \textbf{(2.3.1.14)}$$

where

$$W(q) = \begin{cases} 1, & |q| < w \\ 0, & \text{otherwise}. \end{cases} \qquad \textbf{(2.3.1.15)}$$

The impulse response of the ramp filter is given as:

$$h(t) = \int_{-w}^{w} |q| e^{j2\pi qt} dq = \frac{1}{2\tau}\left(\frac{\sin 2\pi\tau t}{2\pi\tau t}\right) - \frac{1}{4\tau^2}\left(\frac{\sin \pi\tau t}{\pi\tau t}\right)^2. \qquad \textbf{(2.3.1.16)}$$

The frequency representation and impulse response of ramp filter given in figures 2.3.1.2 and 2.3.1.3.

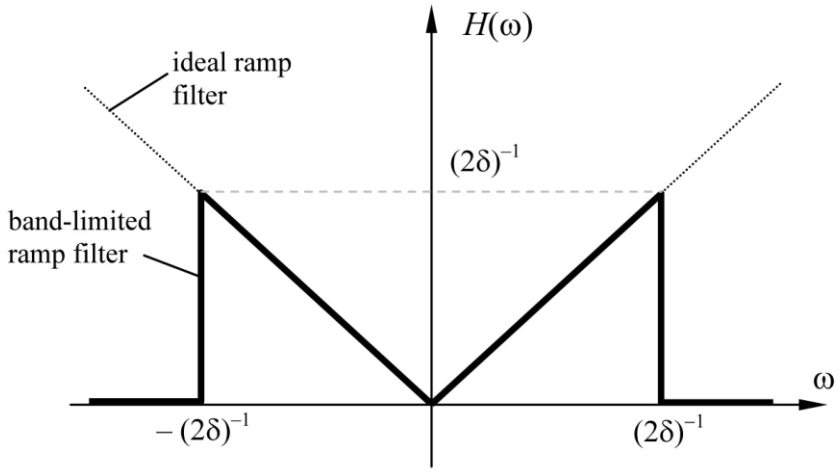

Figure 2.3.1.2 The demonstration of band-limited ramp filter [19].

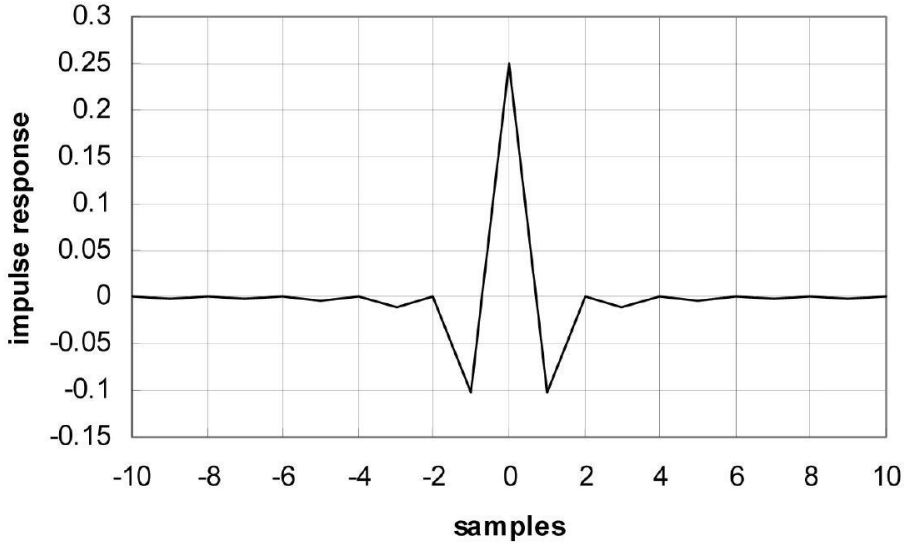

Figure 2.3.1.3 The illustration of the impulse response of ramp filter [19].

As it can be seen in figures 2.3.1.2 and 2.3.1.3, ramp filter suppresses the blurring coming from the backprojection. Indeed, ramp filter works as a derivative filter and enhances the edges. In order to reduce amplification of high-frequency noise present in the image, the window function is used in practice by multiplying window function with original ramp filter in the frequency domain. Thus, the filter becomes softer and artifacts present in the image are reduced. However, the spatial resolution is impaired by smoothing filters. There is always a trade-off between spatial resolution and noise performance of estimated image.

There have been lots of low-pass filters that are used in CT reconstruction. To describe a window function formulation, there are two parameters as cut-off frequency and order of function. The cut-off frequency determines the elimination level and above this level, the frequency is suppressed. The order of filter determines the slope of the filter. The most commonly used window functions' mathematical formulations are given below [30]:

- Hanning filter:

$$\Pi_H(\mathrm{q}) = \begin{cases} 0.5 + 0.5\cos\left(\dfrac{\pi(\mathrm{q})}{q_c}\right), & 0 \le |q| \le q_c \\ 0, & otherwise \end{cases}, \qquad \textbf{(2.3.1.17)}$$

where q and q_c are spatial and cut-off frequencies respectively.

- Hamming filter:

$$\Pi_{HM}(\mathrm{q}) = \begin{cases} 0.54 + 0.46\cos\left(\dfrac{\pi(\mathrm{q})}{q_c}\right), & 0 \le |q| \le q_c \\ 0, & otherwise \end{cases}, \qquad \textbf{(2.3.1.18)}$$

similarly, q and q_c are spatial and cut-off frequencies respectively and produces the smoothest results.

- Shepp-Logan filter:

$$\Pi_S(q) = \frac{2q_c}{\left[\pi(\sin|q|\pi/2\mathrm{q}_c\right]}. \qquad \textbf{(2.3.1.19)}$$

The Shepp-Logan filter generates the sharpest image.

- Butterworth filter:

$$\Pi_B(q) = \frac{1}{\left[1+(\mathrm{q}/\mathrm{q}_c)^{2n}\right]}, \qquad \textbf{(2.3.1.20)}$$

where, n is the order of the filter. The filter is able to both preserve the image resolution and suppress noise due to the capability of changing the cut-off frequency and order of filter at same time.

The selection of window function and cut-off frequency has a significant impact on achieving the desired image. Mostly, design details of the filters are empirical also depend on examination type. The results of different filter functions are given in Figure 2.3.1.4. As can be seen in the figure, ramp and Shepp-Logan results are quite similar while background noise is more present in the images. The Hanning and Hamming low-pass filters provide smoother images. The results acquired with 90 number of projections and $q_c = 0.5$ for all illustrations.

The interpolation needs to be used in FBP either on filtered projections data or on estimated images. In backprojection step, the filtered profile is distributed to closer pixels by using linear or nonlinear interpolations. For ray-driven backprojection, each ray's intensity distributed into pixels which are the closest to the ray. Another way is using pixel-based backprojection which is called pixel-driven back projection. In this method, the ray which goes through the pixel center and intersects it with the filtered profile. Usually, the position of intersection does not correspond to the exact value of the projection. Thus, in order to estimate the value of filtered projection at the intersection position, interpolation methods should be used. The illustration of different backprojection methods is given in Figure 2.3.1.6. The simple forms of interpolation are preferred as nearest neighbor or linear to reduce computational load. To improve the accuracy of interpolation advanced forms can be used such as cubic or spline interpolation methods.

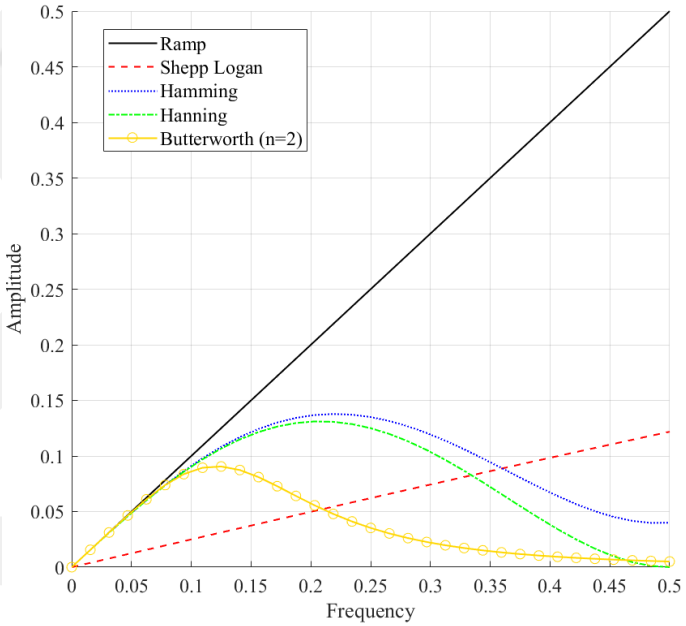

Figure 2.3.1.4 The illustration of ramp and window functions for cut-off frequency $q_c = 0.5$ **and order** $n = 2$.

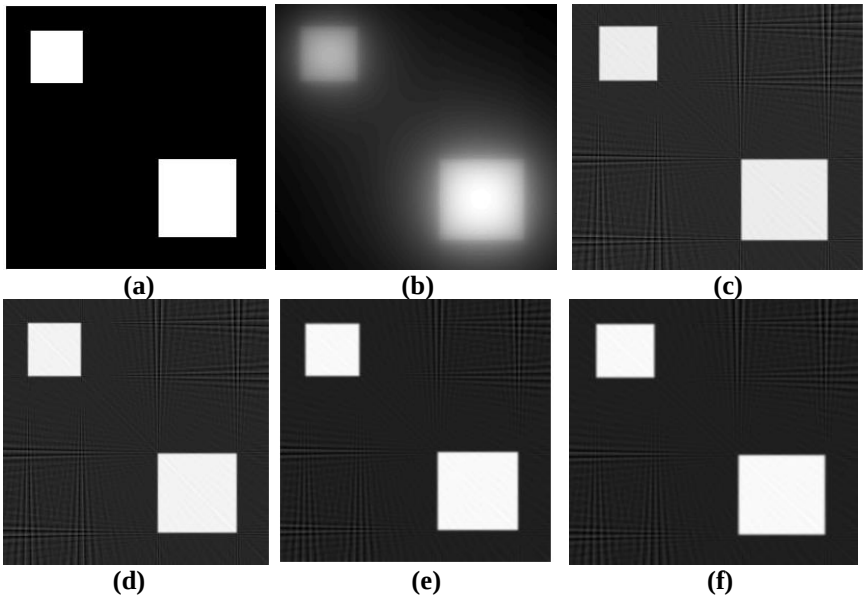

Figure 2.3.1.5 (a) The visualization of true image, (b) simple backprojection, (c) ramp, (d) Shepp-Logan window, (e) Hamming window and (f) Hanning window results.

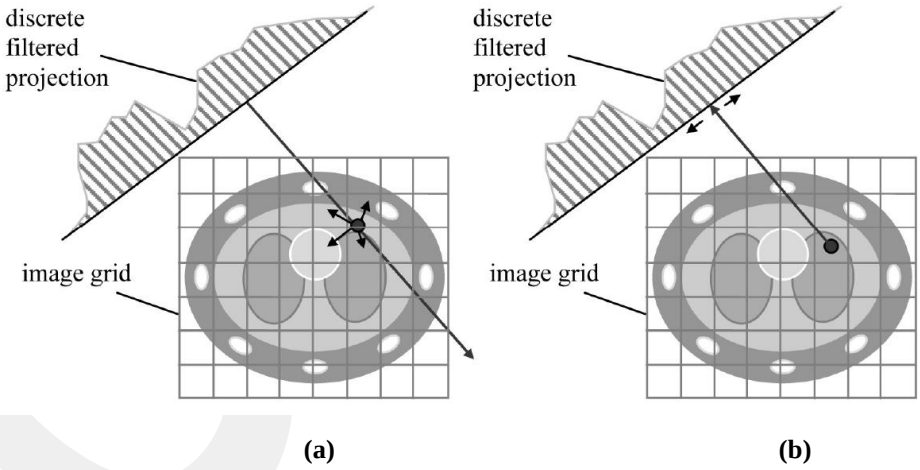

Figure 2.3.1.6 (a) The demonstration of ray-driven and (b) pixel-driven backprojections [19].

2.3.2. Algebraic Reconstruction Technique (ART)

Iterative reconstruction (IR) methods have been developed in CT image reconstruction field due to the inefficacy of analytical methods. However, the computational load of image reconstruction has been increased due to demands

of high image resolution. Thus, the usage of IR methods is limited in the practical application of current systems. However, advancements in computation power lead to IR methods become a hot topic for both clinical and research areas. In literature, there exists many texts explaining the principles of IR methods in details such as Herman (1979) and Kak and Slaney (1988). Kak and Slaney discuss projection and image representation for algebraic methods with visual explanations also elaborate computer implementations of the algebraic method and its forms. The typical IR method can be divided into three major steps as acquiring projections of the object which provides observed raw data. The second step is to compare observed data with real measured raw data to compute correction term. In the last step, the error is backprojected to the object. The steps are illustrated in Figure 2.3.2.1. These three steps are repeated until a certain convergence criterion is a satisfied or maximum number of iteration is reached.

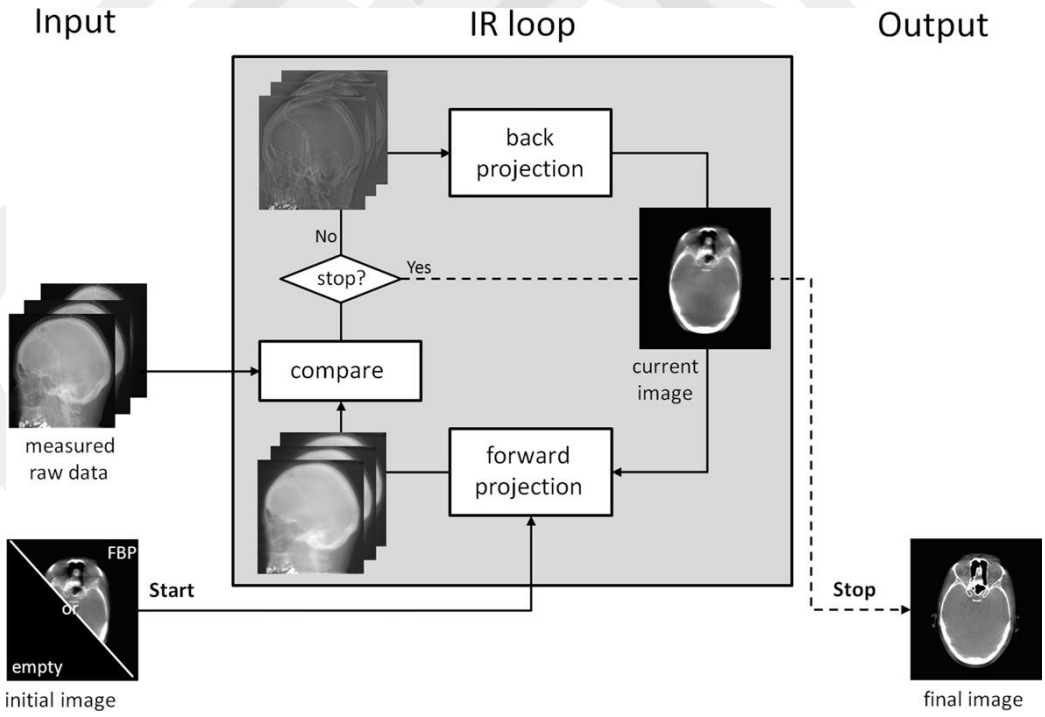

Figure 2.3.2.1 Illustration of the typical IR method. The final image can be estimated from empty or FBP reconstructed initial image [31].

Algebraic reconstruction technique (ART) is the earliest method in the literature of IR techniques also called as Kaczmarz method originated from its

inventor [32]. It was primarily used in image reconstruction by Gordon in 1970 [33]. ART is a reconstruction technique which uses the projections that are provided from different perspectives to estimate the desired object. The implementation of ART as the same as IR methods scheme (Figure 2.3.2.1). The idea of ART is to solve linear equations using detector values and the voxel or pixel contribution to projections. The linear equations are formulated as follows:

$$y_i = \sum_{j=1} a_{i,j} x_j \,, \qquad \textbf{(2.3.2.1)}$$

where the number of the ray is represented with $i = 1, 2, ..., M$, $j = 1, 2, ..., N$ represents the number of pixels in the object and $a_{i,j}$ is weighting parameter which is computed using Siddon's algorithm and indicates the intersection of the pixel with the *ith* ray. y stands for projection value for certain ray and x represents the estimated image intensity. The illustration of the intersection of the X-ray beam and image pixels is given in Figure 2.3.2.2. In order to solve these equations matrix, inversion-based methods can be used. However, an ill-posed system and large volumes are taken into account, iterative methods have been proposed to overcome these issues. The formulation of the method is given as:

$$x_j^{k+1} = x_j^k + \frac{\left(y_i - \sum_{n=1}^{N} a_{in} x_m^k \right)}{\sum_{n=1}^{N} a_{im}^2} a_{ij,} \qquad i = 1, 2, ..., M \;,\; j = 1, 2, ..., N \,, \qquad \textbf{(2.3.2.2)}$$

where x_j^{k+1} and x_j^k represent the estimated image, previous intensity values and updated image by adding the correction term which is computed from the difference between measured ray sum (y_i) and observed ray sum ($\sum_{n=1}^{N} a_{in} x_m^k$). These computations are repeated until a convergence criterion is satisfied.

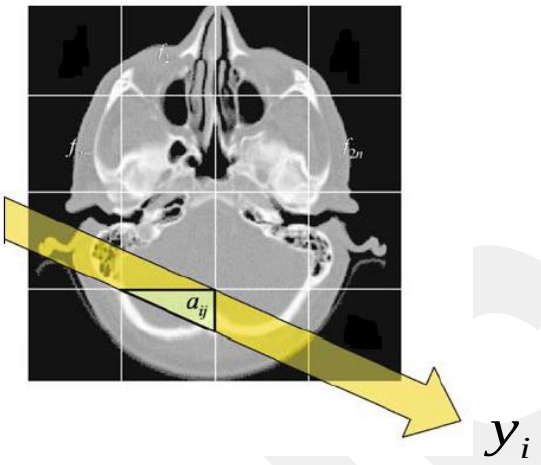

Figure 2.3.2.2 The intersection of X-ray beam and pixels of object. The section of pixel that intersects with X-ray beam included in system equations as weighting term and calculated using Siddon's algorithm [18].

2.4 Compressed Sensing

The Shannon/Nyquist sampling theory states that the sampling frequency needs to be at least twice as much as the highest frequency present in the signal to avoid aliasing [34], [35]. In many practical applications, Nyquist rate is very high such as digital image and video cameras and imaging systems. Thus, the data acquisition and reconstruction become challenging in real applications.

(CS) overcomes these problems by exploiting the sparsity existing in the data or by sparsifying it. CS theory on creating an efficient sensing approach that involves the crucial information inserted in a sparse and small number of data [36]. Thereby, CS theory is able to reduce the number of data that need to be stored and computed. By using fewer samples, CS can accurately recover signal or an image using the sparsity principle. This approach is very useful in imaging modalities such as MRI and CT. Especially in CT image reconstruction, the main issue is to estimate an image accurately from insufficient projection data. The acquisition of data can be formulated by linear equations as follows:

$$y = Ax\,, \qquad \textbf{(2.4.1)}$$

where y is the vector of measurements in $\mathbb{R}^m$, x is the image to be reconstructed in $\mathbb{R}^n$ and A denotes the $m \times n$ system matrix. The CS method enables the accurate reconstruction from $m \ll n$ (indicates the underdetermined system) situation [36] using the advantage of the sparsity of signals.

The entire concept of CS consists of three steps: encoding, sensing and decoding [37]. In the first step, the image x is encoded in a small vector by a system matrix. The second step is to gather a few data y. The third step is to recover x from y underdetermined measurements. The more realistic solution is minimizing ℓ_1 norm of the sparse image [38]. Some natural images and signals are sparse by itself or can be done sparse by taking magnitude of the image's gradient [39]. The constraint minimization problem can be expressed as given below and ψ is sparsifying operator:

$$\min \|\psi x\|_1, \; subject \; to \quad y = Ax. \tag{2.4.2}$$

2.4.1 Total Variation

The most popular method of CS is total variation (TV) and there exists a number of variants of TV minimization algorithm in literature. TV has been used as a regularization term in inverse problems and was proposed by Rudin, Osher, and Fatemi [40]. TV minimization is frequently used in image processing applications as an efficient filtering operator.

TV is a numeric value that indicates how much rapid variation occurs between the neighboring pixel values. High total variation corresponds to the excrescent details and usually noise present in the image because tomographic images have generally uniform intensity values in the organ structures and rapid variations occur at only the edges of structures [14]. In the light of this information, minimizing TV of the CT image in order to rid of undesired details while preserving the edges. TV of a 2D image can be defined as follows:

$$TV(X) = \sum_i^K \sum_j^L \sqrt{\left(\left(X_{i,j} - X_{i-1,j}\right)^2 + \left(X_{i,j} - X_{i,j-1}\right)^2\right)} \quad , \qquad \textbf{(2.4.1.1)}$$

where X represents an image to be reconstructed and $X_{i,j}$ represents intensity value at pixel (i, j) *with* $i = \{1, \ldots, K\}$, $j = \{1, \ldots, L\}$. Since the present Chapter focuses on 2D image reconstruction, Table 2.4.1.1 summarizes the reconstruction techniques reviewed until here.

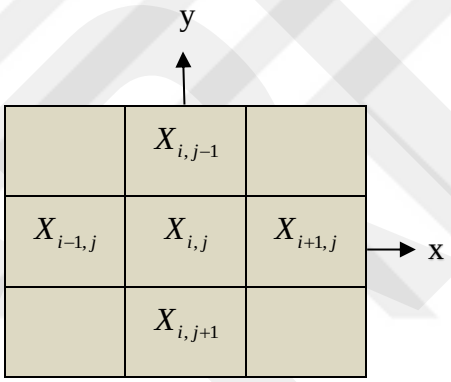

Figure 2.4.1.1 The illustration of TV formulation on neighbor pixels.

	FBP	ART	TV
Reconstruction time	low	high	medium
Accuracy	low	medium	high
Reconstruction ability from insufficient data	low	medium	high
Noise sensitivity	high	medium	low

Table 2.4.1.1 Comparison of CT reconstruction methods.

Chapter 3

Total Variation Regularized Iterative Filtered Backprojection for Sparse CT Imaging

3.1 Related Work

The main knowledge of CT image reconstruction can be divided into two major groups as direct (analytical) and iterative reconstruction techniques. Despite recent works focus on iterative methods, the commercial CT scanners still employ one of the analytical method FBP. FBP is a direct approach which is based on estimating the Fourier Transform (FT) of objects from their projections in the frequency domain, then obtaining the spatial distribution of the object [41], [42]. Related to the FBP reconstruction methods, the works can be enclosed in two main topics as exploring new interpolation methods or filtering operators to increase the accuracy of reconstruction.

In order to eliminate shortcomings of traditional ramp filter, the paper which is titled as ‘ A Novel Scheme to Design the Filter for CT Reconstruction Using

FBP Algorithm' [43] proposes a novel scheme to create new filters to use in FBP reconstruction instead of traditional ramp filter. The performance evaluation of designed filter clearly outperforms to ramp filter. With similar objective, the article titled 'Adaptive Filtered Back Projection for Computed Tomography' [44] proposes an adaptive linear filter based on 2D kernels as a post-processing step in image reconstruction. Their aim is to avoid usage of iterative methods due to their computational burden. Their results show that the adaptive scheme effectively increases the reconstruction quality. A paper appeared in 2013, 'Improving Filtered Backprojection Reconstruction by Data-Dependent Filtering' [45] gives an approach for 2D parallel-beam reconstruction problems. The paper introduces a new approach which is called minimum residual filtered backprojection method in the paper. The method drives a data dependent filter to minimize the projection error using the sense of algebraic methods. The results are compared with algebraic methods and the results similar to the one of algebraic methods which shorter reconstruction time.

Another study on filter design with regard to interpolation is 'Filter Design for Filtered Back Projection Guided by Interpolation Model' [46] introduces an approach that combines ramp filtering and spline interpolation into a new filtering operator. The designed filtering operation is applied to sinogram and improves the reconstruction quality even at low interpolation degrees which provides faster reconstruction. In the similar sense, the paper titled 'Optimal Prefiltering for Linear Interpolation in Computed Tomography' [47] aims to illustrate the modern interpolation models for obtaining more accurate results. Linear interpolation is widely used in the backprojection step of CT reconstruction because it is able to provide a balance between computation time and accuracy. In a related paper, a proper pre-filter is applied to projection data and it increases the accuracy of current image reconstruction method. The recent study is titled as 'Optimal Filtered Backprojection for Fast and Accurate Tomography Reconstruction' [48] formulates the optimization scheme for filtering of backprojection and also connects the optimization of filtering and filtering- backprojection approach.

The ‘A Novel Iterative CT Reconstruction Approach Based on FBP Algorithm’ [49] introduces iterative FBP by reducing the difference between original projection data and reprojection data which is generated by forward projection of the reconstructed image by FBP. In every iteration, the difference between original and reprojection data is filtered and smeared back to produce correction term. The correction term is added to the reconstructed image by FBP. The simulations support the superiority of proposed method to some IR methods.

As it can be seen there is not a certain step to be optimized but several steps of FBP process can be improved. Most of the studies relevant to FBP enclosed in interpolation and denoising steps.

However, the performance of FBP is not sufficient when the projection data is noisy or limited number of projections are available. In this case, IR methods have been proceeded to estimate object from projections more accurately since 1970s [50]. One of the earliest iterative method ART solves the linear equations using sets of measured and observed projections [50]. Applications of varied forms of ART such as simultaneous algebraic reconstruction (SART) has provided superior results to traditional ART reconstruction method [51]. Another type of iterative methods is least squares technique (ILST) that is based on statistical methods [52]. Because of data insufficiency in low dose CT imaging, the new approaches have been developed to overcome reconstruction problem such as TV minimization. Despite TV minimization is proposed by Rudin, Osher, and Fatemi in 1997, TV has been improved and used in image reconstruction field as a strong tool. The method has been evaluated for handling data inadequacy, limited angle and bad bins problems of CT imaging in 2009 [14]. In the early work of Quinto indicates that boundaries and details of the object are more accurately recovered through projection directions. Moreover, the artifacts present only in some certain directions [53]. To address this issue, anisotropic TV has been introduced in the literature [54], [55]. In their study, it is clearly seen that edges and artifacts are apparent at specified directions while in other directions they are less present.

Another limitation of TV minimization is that it is based on local neighboring pixels or voxels. Local TV minimization utilizes constant penalization without considering spatial intensity variations. In order to increase contrast and accuracy also preserving detailed structures of reconstructed images, non-local TV minimization (NLTV) has been proposed in the literature [56]–[58]. The NLTV presents a non-local TV minimization operator by considering global information.

The previous works of both analytical and IR based methods have been reviewed. The weaknesses and advantages of the reconstruction methods have been outlined in this Section.

3.2 The Problem Definition

Since the certain range of view angle is missing in sparse CT imaging, the quality of the image will be affected and degraded. Thus, in sparse tomographic imaging, the main challenge is to reconstruct images without noticeable limited-view artifacts arose from the insufficient projection data [14]. Iterative techniques have been used for improving image quality while diminishing the required number of projection in CT imaging. However, the significant weakness of IR techniques is a vast computational burden because of high computational complexity.

The first contribution of present thesis centers on how to solve an ill-posed problem in low dose CT imaging by exploiting computational efficient method FBP and superior features of the TV minimization. The ultimate purpose of the proposed algorithm is to reconstruct a CT image which is comparable to the outcome of the IR techniques such as ART [59] while keeping its computational load as low as being able to use in clinical applications.

3.3 Application of Proposed Method

Our iterative reconstruction algorithm consists of two major parts as FBP and TV minimization. The ingredients of FBP and TV minimization methods, as well as the integration within the CT imaging system, have been discussed in Chapter 2.

The main component of FBP is 1D filter function. The adjusting parameters of the filtering step are crucial. In such a way that, determining the window function [60] and optimizing the cut-off frequency (q_c) are important factors for reducing noise while keeping the loss of resolution at least [30]. The ramp filter is applied to the projections before backprojection step to reduce low-frequency artifacts. However, the main weakness of ramp filtering is amplifying noise as its gain increases at higher frequencies. In order to suppress high-frequency noise, a proper window function needs to be used. Because of its success in the literature, Hamming window function is used in this work [61]. The cut-off frequency of proposed method is determined by minimizing error based on quality metrics and optimized for a different number of projections. The illustration of filters at $q_c = 0.5$ is showed in Figure 3.3.1 and the form of $W(q)$ determines the suppressing level of filtering.

However, if the problem is overly underdetermined the FBP lacks of providing satisfactory outcomes even if it is computationally so efficient. Thus, exploiting the computationally efficient method FBP and applying TV minimization to get rid of the blurring and other artifacts existing in the images reconstructed by the FBP helps to obtaining superior results using the proposed method. TV minimization has successful applications in limited view angle

imaging through removing artifacts while preserving boundaries and other fine details [62].

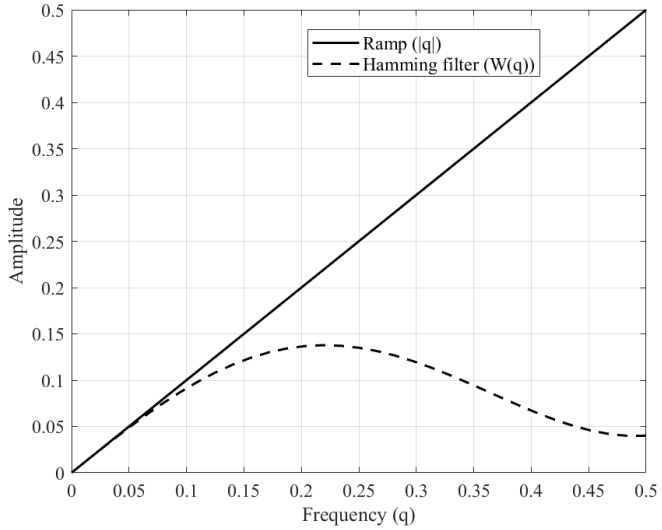

Figure 3.3.1 The illustration of ramp and Hamming filters at $q_c = 0.5$.

TV operator is applied to the FBP reconstructed images in an iterative manner. The formulation is as follows:

$$X^{TV} = \arg\min_{X^{TV}} \left[\left\| X - X^{TV} \right\|_{\ell 2}^2 + \lambda \left\| TV(X) \right\|_{\ell 2} \right], \tag{3.3.1}$$

where X represents the estimated image by FBP, λ is a constant TV regularization term and TV (.) is TV minimization operator. TV of the 2D image can be formulated as l_2-norm of the gradient of the image as:

$$TV(X) = \sum_x^K \sum_y^L \sqrt{\left(\left(X_{x,y} - X_{x-1,y} \right)^2 + \left(X_{x,y} - X_{x,y-1} \right)^2 \right)}, \tag{3.3.2}$$

where X represents an image to be reconstructed and $X_{i,j}$ represents intensity value at the pixel $\{x, y\}$ with $x = \{1,...,K\}$, $y = \{1,...,L\}$. TV minimization is utilized using the gradient descent minimization algorithm.

The flow of the method is given in Figure 3.3.2. The projection data are obtained by the Radon transform. Then, the data are filtered in the frequency domain using the ramp and Hamming filters to improve the quality of low dose CT images by removing the high-frequency artifacts. Then, the initial reconstructed image (the reference image), X^0, is obtained by the inversion of Radon transform. The FBP is used to reconstruct the image (Y^k). The updated image is obtained by $X^{k+1} = X^k + X^0 - Y^k$. Finally, TV minimization is applied to the image X^{k+1}. This procedure is repeated until a number of iteration is satisfied. The pseudo code of given algorithm as below:

Iterative Algorithm of Proposed Method

Input: Load phantom image

Step 1. For each angle acquire projections (forward projection)

Step 2. Compute X^0 using the FBP

k=0;

Step 3. **For** each iteration

For each angle

Forward projection of X^k

End each angle

$Y^k \longleftarrow$ Reconstruct image using the FBP from the forward projection of X^k

Compute $X^{k+1} \longleftarrow X^k + X^0 - Y^k$

Set λ (regularization impact of TV)

$X_{TV}^{k+1} \longleftarrow TV(X^{k+1})$

Compute quality metric values of X_{TV}^{k+1}

k=k+1;

End each iteration

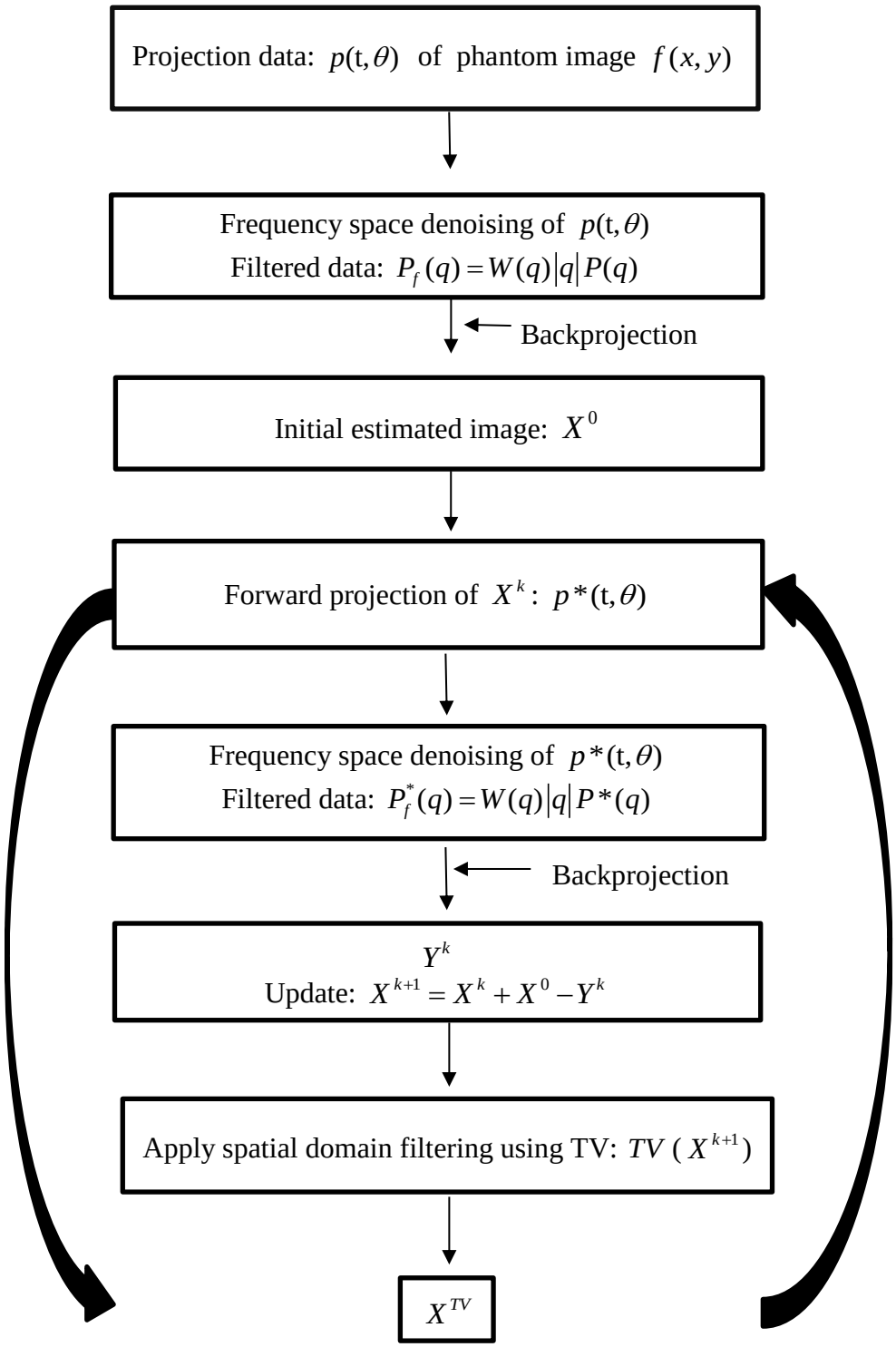

Figure 3.3.2 The flow of the implementation of the proposed method.

3.3.1 Phantom

In order to investigate the performance of the proposed method, the well-known 2D Shepp-Logan phantom model is used. The phantom was designed by Larry Shepp and Benjamin F. Logan for their study [63]. The phantom is a grayscale image that has one large ellipse which illustrates the brain containing other smaller ellipses represent structures of the brain. It has been widely used for testing of image reconstruction algorithms. It consists of ten ellipses and its parameters are given in Table 3.3.1.1. In the present thesis, the modified Shepp-Logan phantom is used due to improved contrast and better visual perception.

Ellipse	**Centre**	**Major Axis**	**Minor Axis**	**Theta**	**Gray Level**
a	(0,0)	0.69	0.92	0	2
b	(0, −0.0184)	0.6624	0.874	0	−0.98
c	(0.22,0)	0.11	0.31	−18°	−0.02
d	(−0.22,0)	0.16	0.41	18°	−0.02
e	(0,0.35)	0.21	0.25	0	0.01
f	(0,0.1)	0.046	0.046	0	0.01
g	(0, −0.1)	0.046	0.046	0	0.01
h	(−0.08,−0.605)	0.046	0.023	0	0.01
i	(0, −0.605)	0.023	0.023	0	0.01
j	(0.06,−0.605)	0.023	0.046	0	0.01

Table 3.3.1.1 The parameters of ellipses that form the Shepp-Logan phantom image.

Figure 3.3.1.1 The Modified Shepp-Logan phantom image with resolution 256×256.

3.3.2 Image Quality Assessment

In order to examine the accuracy of the implemented algorithm, quantitative and qualitative measurements are used. The qualitative measurements are based on visual inspections and do not express a numerical value. Thus, four different quantitative metrics are used in this study. The quantitative metrics aim to measure the similarity between the original phantom image and the estimated image by the proposed algorithm. Root Mean Squared Error (RMSE) is frequently used in medical imaging to compare the reconstructed image with ground truth image. Signal to noise ratio (SNR) measures the reconstructed image noise performance by comparing the estimated image with noise level present in the reconstructed image. Despite the implementation of these metrics is easy, they express the real quality of estimated images at some extent. Thus, a contrast to noise ratio (CNR) and structural similarity (SSIM) are used to validate numerical results in this study.

3.3.2.1 Root Mean Squared Error (RMSE)

RMSE value is widely used for measuring the difference between estimated values by a predictor model and actual values. In medical imaging, RMSE value gives the accuracy or similarity of two images that are predicted image and phantom image. In other words, RMSE shows the convergence rate of the proposed method.

$$RMSE = \sqrt{\sum_{x,y}^{J,K} \left(P_{x,y} - X_{x,y} \right)^2 / N} \,, \qquad \textbf{(3.3.2.1.1)}$$

where N shows the number of pixels, x, y represent the pixel indices and P and X indicate the original phantom image and reconstructed image, respectively.

3.3.2.2 Signal to Noise Ratio (SNR)

Quantitative analyses also include SNR which expresses power of the signal and power noise in medical images. SNR usually states in decibels (dB). SNR gives clues about the noise level of reconstructed images. In our study, the Frobenius norm of the estimated image is used as indicated with the following expression:

$$SNR = 10 \times \log \left(\frac{\sqrt{\sum_{x,y}^{J,K} \left| X_{x,y} \right|^2}}{\sqrt{\sum_{x,y}^{J,K} \left| P_{x,y} - X_{x,y} \right|^2}} \right), \qquad \textbf{(3.3.2.2.1)}$$

similar with RMSE, x, y represent the pixel indices and P and X indicate the original phantom image and reconstructed image, respectively. SNR results turned out to be an inverse form of RMSE values.

3.3.2.3 Structural Similarity (SSIM)

Despite the easy implementation of SNR and RMSE, they may not give successful results when the investigating the visual quality of reconstructed images. For this reason, characteristic of human vision system implementation is developed in the literature [64].

The structural similarity (SSIM) index is an effective method to measure the structural similarity between two images. SSIM computes the similarity based on three features and y local areas that are located in the same regions of images to be compared. The features are the similarity of luminances ($l(\rho,t)$), the similarity of contrasts ($c(\rho,t)$) and similarity of structures ($s(\rho,t)$) [65]. The formulation of the method as follows:

$$SSIM_I(\mathrm{x},\mathrm{y}) = l(x,y)c(x,y)s(x,y) = \frac{\left(2\mu_x\mu_y + c_1\right)\left(2\sigma_x\sigma_y + c_2\right)\left(\sigma_{xy} + c_3\right)}{\left(\mu_x^2 + \mu_y^2 + c_1^2\right)\left(\sigma_x^2 + \sigma_y^2 + c_2^2\right)\left(\sigma_x\sigma_y + c_3\right)}. \quad \textbf{(3.3.2.3.1)}$$

In the formulation μ_x and μ_y values represent the mean of the intensity of x and y patches, σ_x and σ_y indicate the standard deviation of them. The formulation of c_1 and c_2 is given below.

$$c_m = (K_m L)^2, \quad m = 1,2, \quad \textbf{(3.3.2.3.2)}$$

where L is the dynamic range of the input image (for 8 bits grayscale image L equals to 255) and $K_m \ll 1$ for $k = 1,2$ are constants. In this work, we employee

the global structural similarity for the proposed method at last iteration since other metrics suggest us the proposed method is superior to other reconstruction methods notably.

3.3.2.4 Contrast to Noise Ratio (CNR)

The noise present in medical images degrades the image quality. In order to measure that, CNR has been developed similar to SNR and defines the ability to differentiate the small details in medical images against to noise. CNR values are computed only for proposed method since other metrics suggest us the proposed method is superior to classical FBP notably. CNR values are computed by using the following notation:

$$CNR = \left(\mu_o - \mu_b \right) / \sigma_b \ , \qquad \textbf{(3.3.2.4.1)}$$

where the mean intensity of the targeted structure is presented as μ_o, μ_b is the mean intensity of background and σ_b is the standard deviation of background noise in the ROI. The ROI is framed in a white rectangle with Figure 3.3.2.4.1 below.

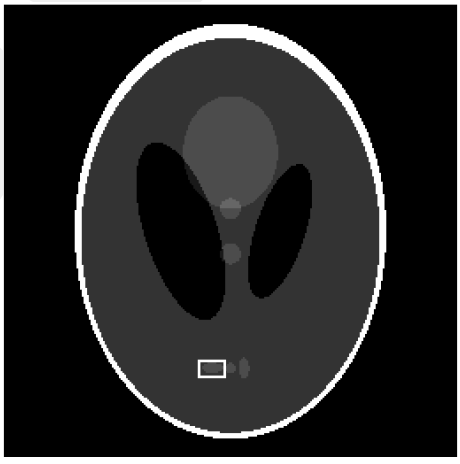

Figure 3.3.2.4.1 The illustration of the targeted region to investigate CNR values from reconstructed images by the proposed method.

3.4 Simulation Results

The performance of the proposed method is examined using 2D modified Shepp-Logan phantom in [0-1] dynamic range with 256×256 resolution and all simulations are performed in MATLAB® 2017a software with Intel Core i7 6500U / 2.5 GHz CPU and 8 GB RAM computer. In the study, the parallel beam geometry is simulated. The scanning angle is 180° for three different setups with 30, 40 and 60 projections. The simulated projection data is provided by forward projection of original phantom image without any noise added.

The FBP and TV minimization algorithms have parameters that affect the performance of proposed method. The cut-off frequency parameter is optimized separately for each projection setup and fixed to a constant value. The TV regularization parameter (λ) which determines the balance between the level of noise existing in the estimated image and preserving edges and is fixed to 1 based on previous knowledge. The interpolation type used in backprojection step is selected as linear.

The results are analysed both qualitatively and quantitatively. The parameters used in the simulations are summarized in Table 3.4.1.

As the simulations are performed using insufficient projection data, several artifacts are observed in the reconstructed images. In order to compare visually the results of the proposed method with original phantom and BP and FBP methods, the reconstructed images at the first iteration are given in Fig. 3.4.1 (a). The FBP is able to estimate only the main features of the phantom as well as some small details to some extent especially when the number of projections increased. The proposed method provides improved results even at the smallest number of projections. As the number of projections is increased, the method provides much better results by recovering even the tiniest details.

Reconstructed images at the final iteration can be seen in Fig. 3.4.1 (b). Streaking artifacts in the FBP results is still present while the proposed method

helps obtain superior results by suppressing background noise and generating sharper images. Almost all details are fully recovered by the proposed method when the number of projections is 40 or more. To further analyze the visual difference between the FBP and the proposed method, vertical and horizontal profiles of the reconstructed images are drawn in figures 3.4.2. and 3.4.3.

Parameter	Value
Resolution	256×256
The motion of X-ray	Step-and-Shoot
Projection Geometry	Parallel-Beam
Scanning Angle	180°
Number of Projections	30, 40 and 60
Iteration Number	50
TV Regularization Parameter	1
Window Function	Hamming
Cut-off Frequency	0.4, 0.6 and 1

Table 3.4.1: Simulation parameters of the proposed method.

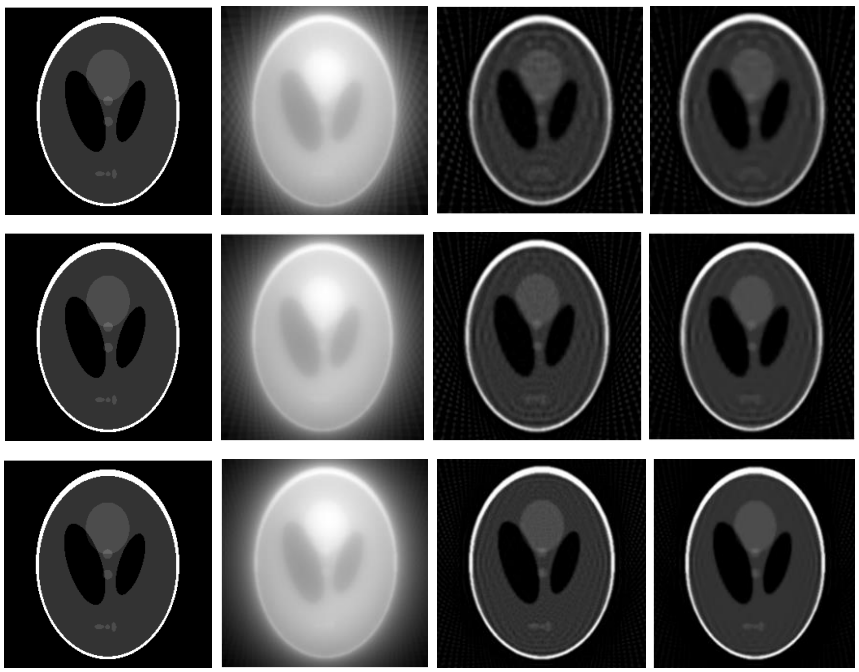

(a)

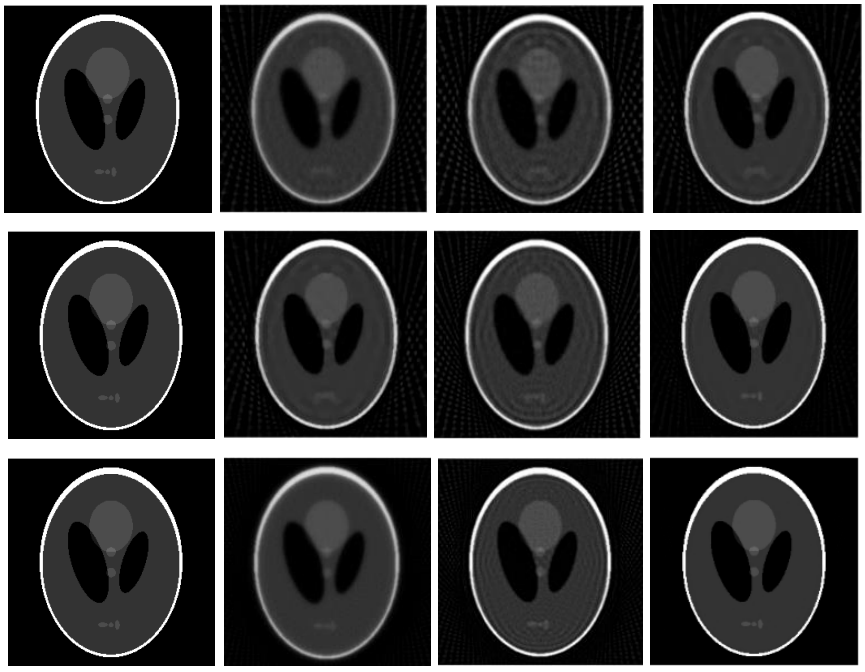

(b)

Figure 3.4.1 (a) The reconstructed images at the first iteration and (b) at the final iteration. From left to right column: original image and the reconstructed images by using BP, FBP and proposed method, respectively. The first row: estimated images by using 30 projections, the second row: estimated images by using 40 projections, the third row: estimated images by using 60 projections.

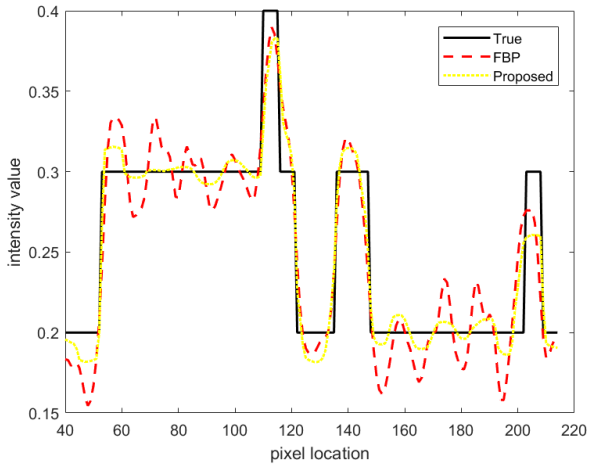

(a)

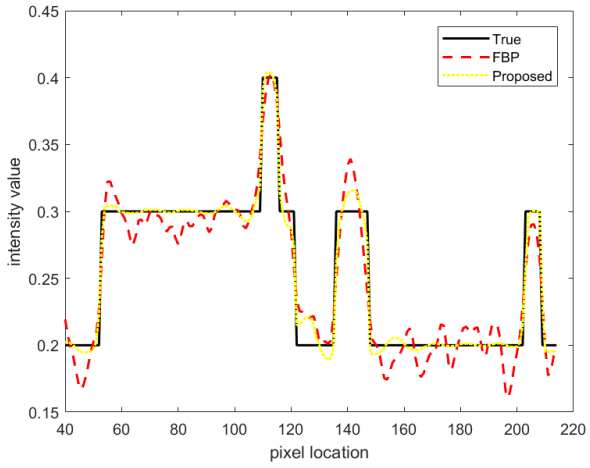

(b)

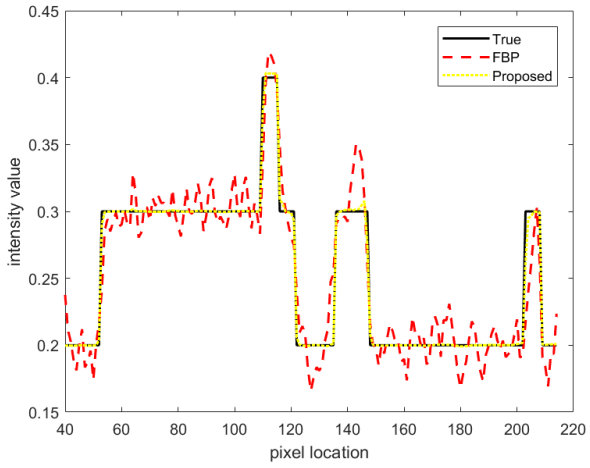

(c)

Figure 3.4.2 Vertical profile drawn at the 128th column, from 40th row to 214th row of the original phantom, reconstructed images by FBP and the proposed method. (a) The profile using 30 projections, (b) using 40 projections, and (c) using 60 projections.

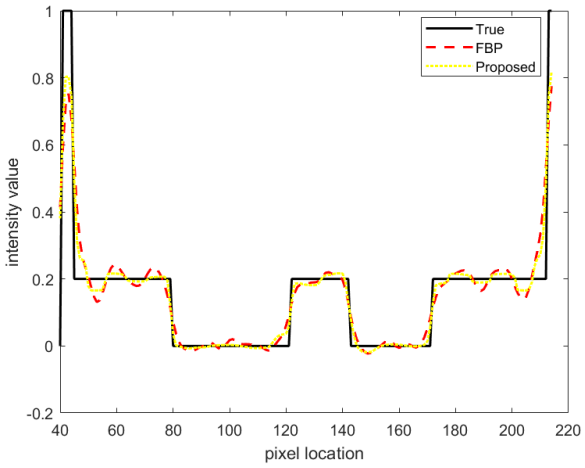

(a)

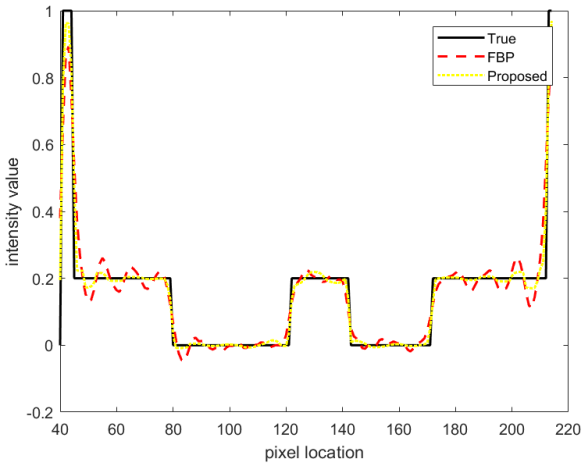

(b)

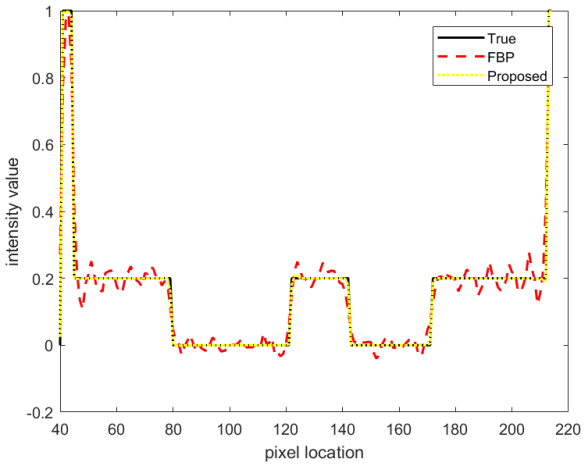

(c)

Figure 3.4.3 Horizontal profile drawn at the 128th row, from 40th column to 214th column of the original phantom, reconstructed by the FBP and proposed method. (a) The profile using 30 projections, (b) using 40 projections, and (c) using 60 projections.

The horizontal profile is drawn at 128th row, from 40th column to 214th column and vertical profile is formed using vice versa direction of the horizontal profile. The FBP shows severe oscillations due to insufficient projection data whereas the proposed method is able to track nearly the original profiles in both directions. The oscillations are removed utterly by the proposed method in 60 projections. The intensity profiles of proposed method show sharper transitions in edge regions also more similar to the true image.

In order to validate results of the visual analysis, the numerical analyses are performed on outputs of BP, FBP, and the proposed methods. The performance comparisons are done using RMSE, SNR, CNR and SSIM metrics for each projection setup. As can be noticed from figures 3.4.4 and 3.4.5, the results of BP nearly become the same as the results of FBP while the FBP results remain stable as expected. Starting from this point, thanks to our update step in an iterative algorithm, BP can generate such results that are comparable with the FBP results. This is an unexpected outcome because the BP method is free of adjusting filter parameters such as window function and cut-off frequency.

Clearly, the results of proposed method have the lowest error level and the highest noise removal ability in regard to RMSE and SNR values respectively. Beside this, TV-based methods can lead to loss of small details in reconstructed images. However, our method clearly recovers all details in the reconstructed images with sufficient robustness against to noise.

CNR and SSIM values are computed only for the proposed method because of the superiority of RMSE and SNR values of the proposed algorithm. The reconstructed ROI to calculate CNR values for a different number of projections are given in Figure 3.4.6.

Moreover, 300% zoomed images of the targeted area which contains fine details are shown in Fig. 3.4.7 to have a detailed visual investigation of reconstructed images. As expected, increased number of projections helps to obtain improved image quality.

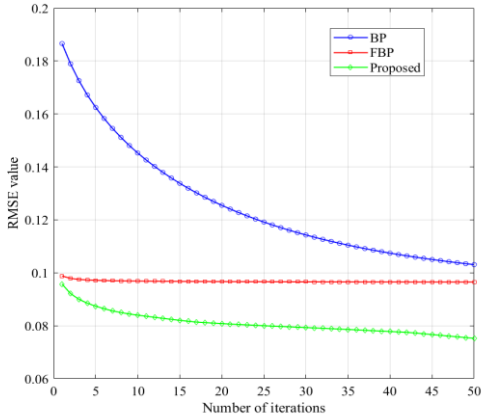

(a)

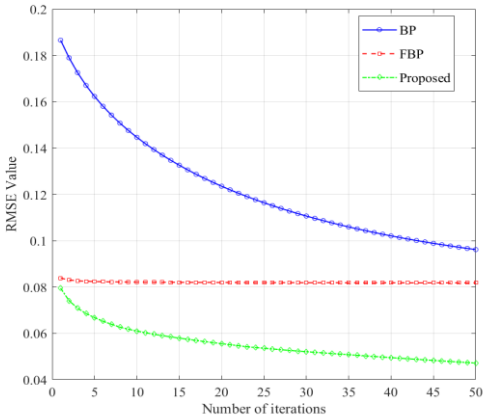

(b)

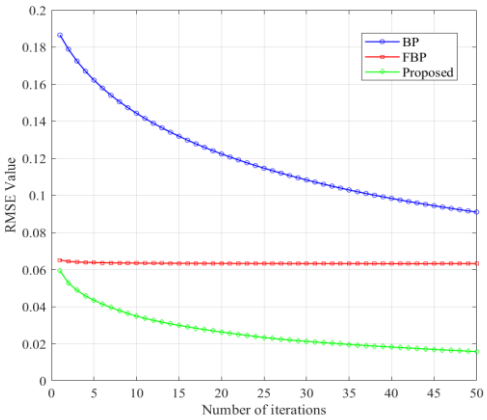

(c)

Figure 3.4.4 RMSE values of BP, FBP and proposed method for different projection setups, (a) RMSE graph of 30 projections, (b) RMSE graph of 40 projections and (c) RMSE graph of 60 projections.

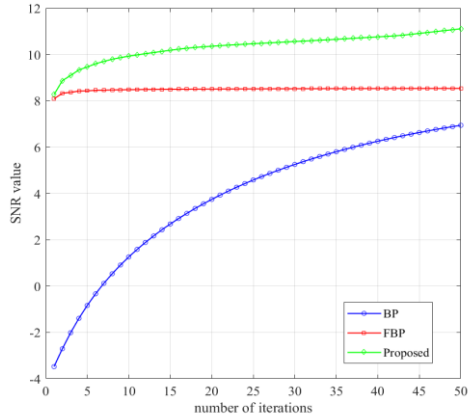

(a)

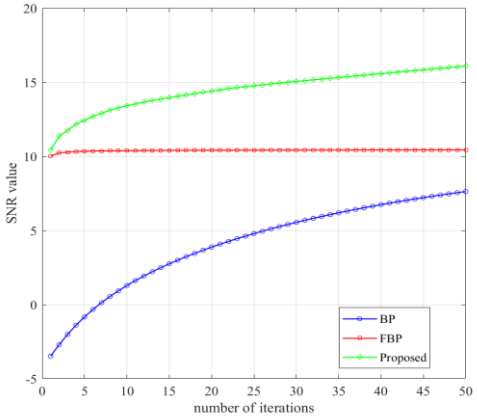

(b)

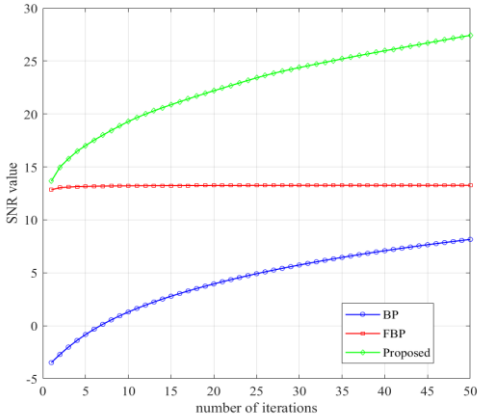

(c)

Figure 3.4.5 SNR values of the BP, FBP and proposed method for different projection setups, (a) SNR graph of 30 projections, (b) SNR graph of 40 projections and (c) SNR graph of 60 projections.

In clinical practice, having the ability of recovering small details is critical to detect accurately low-contrast small lesions. The zoomed images clearly show the ability of the proposed method to recover fine details by removing severe artifacts due to incomplete projection data.

All numerical analyses for the proposed method in the last iteration are demonstrated in Table 3.4.2 to quantify the performance of proposed method with algebraic reconstruction technique [59], [66]. The results validate that the proposed algorithm is a computationally efficient way to generate images comparable to the results of ART using insufficient projection data.

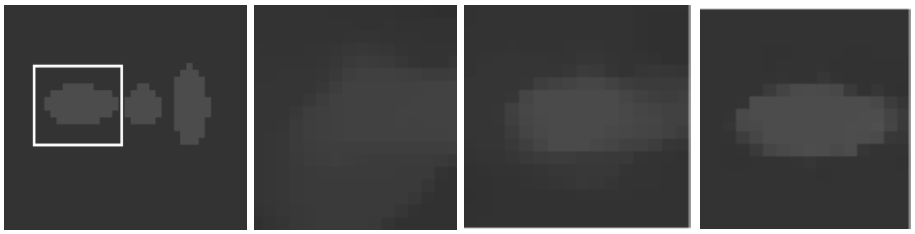

Figure 3.4.6 The illustration of targeted regions to investigate CNR values from reconstructed images by the proposed method using 30, 40 and 60 projections. From left to right: the targeted structure enframed in the original image and reconstructed images using 30, 40 and 60 projections respectively.

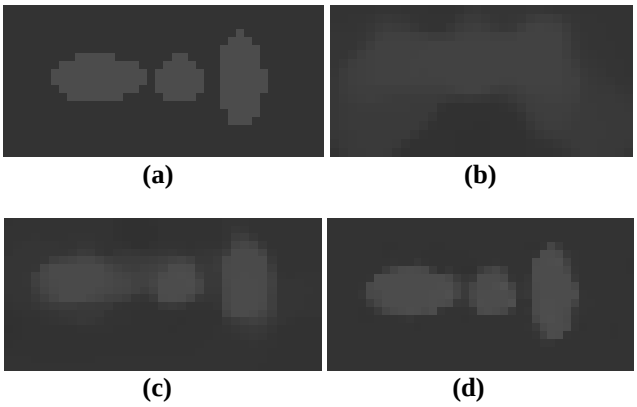

Figure 3.4.7 300% zoom of a region in the original image which has small details. (a) Original image, (b) reconstructed image of the proposed method by using 30 projections, (c) 40 projections and (d) 60 projections.

	RMSE	SNR	CNR	SSIM
30 Projections	0.075	11.106	13.896	0.55
40 Projections	0.047	16.097	17.228	0.73
60 Projections	0.016	27.428	22.880	0.99

Table 3.4.2 Numerical results of the proposed method at last iteration.

3.5 Discussion and Outlook

In medical imaging area, lowering radiation dose and producing acceptable quality images in limited time have been demanded frequently. The aim of this study relies on the similar idea that obtaining comparable results of ART [59] by combining the computational efficiency of the FBP and superiority of TV minimization in sparse CT imaging. The quantitative results are quite encouraging that the proposed method provides comparable results with the results of ART when the number of projections exceeds 30. Since the major problem with ART is its high computational time in contrast to the FBP, we develop an efficient algorithm for sparse CT imaging.

The method presented in this thesis requires much less time compared to ART as can be seen from Figure 3.5.1 and the proposed method provides comparable results, if not better, with ART. For example, the proposed method for 60 projections provides better results such as 27.4 SNR and 0.016 RMSE values than ART which gives 20.9 SNR and 0.031 RMSE values using 60 projections. The similarity metric indicates the superiority of the proposed method

through producing SSIM number of “0.99” whereas ART gives a SSIM value of “0.94”. All quantitative metrics show consistent results for the proposed method.

The proposed method depends on adjusting three parameters as TV regularization parameter λ, window function, and cut-off frequency. For the regularization parameter λ, an experienced-based constant value is used for all simulations. The determination of cut-off frequency is highly dependent on number of projections. When the number of projections increases from 30 to 60, the cut-off frequency is increased from 0.4 to 1 as expected due to noise is minimized with the increased projections. The appropriate window function is varied according to object structure to be scanned.

Although the number of iterations is limited to 50, the trend of numerical graphs suggests gradually increase the performance of the proposed method.

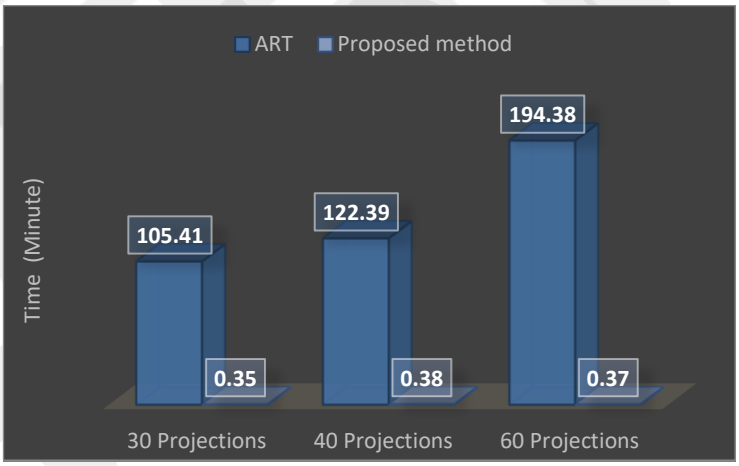

Figure 3.5.1 Reconstruction time in minutes for a different number of projections by using ART and the proposed method.

Chapter 4

Magnetic Nanoparticles for CT Imaging as Contrast Agents

4.1 Background

As discussed throughout the present thesis, CT is the most widely used non-invasive imaging modality in clinal imaging due to striking benefits. The major components of a typical CT scanner are an X-ray tube and detector array as can be seen in Figure 4.1.1. While the detector array and X-ray tube are rotated synchronously around the patient, the intensity of X-ray radiation is reduced. X-ray beam goes through the object and two main interactions are observed as scattering and absorption. The detector array records the attenuated X-ray beams to form projection data from different angles.

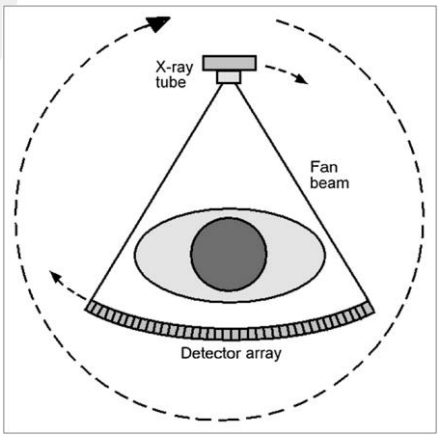

Figure 4.1.1 The schematic representation of a CT scanner (third generation) [67].

4.1.1 Principle of Contrast Generation

Since the detailed information about the interaction of X-ray with matter is given Chapter 2, in this section we just focus on the underlying principle of contrast generation of CT imaging.

In medical imaging applications, the X-ray tube voltage is in 80-140 kV range that defines the maximum limit of X-ray photons. The energy of X-ray photons typically ranges from 20 keV to maximum of X-ray tube voltage (140 keV). Low energy photons below the 20 keV are usually absorbed by body structures thus they do not reach to the detector. In 20 keV-140 keV energy range, there are two main interactions as the photoelectric and Compton effects.

Basically, contrast enhancement in CT imaging is mainly due to the photoelectric effect. The photoelectric effect defines the situation that the photon has greater but nearly the same energy with the binding energy of an electron. Thus, the X-ray photon usually transfers entire energy to K-shell electron and the electron is ejected then called as photoelectron. The binding energy of human tissue is very low (approximately 500 eV). Thus, the photoelectron travels a short distance roughly as long as the dimension of the human cell before totally attenuated [19]. The strongly bounded electrons lead to more photoelectric absorption (K-shell). The photoelectric effect is proportional to the atomic number cubed (Z^3) and reduces with increased photon energy (E^3). Therefore, using high atomic number elements leads great differences in absorption rate of X-rays and results in contrast enhancement.

The photoelectric effect generates high-quality images at low energy X-rays since no scattering radiation is observed. The variations in probability of photoelectric effect underlie the contrast generation between different tissues [19]. However, it leads to high radiation exposure to patient whereas high-energy X-rays (Compton effect) results in degradation in contrast. Thereby, there is a trade-off between image quality and radiation exposure [68]. An adequate increase in energy of X-ray radiation can increase the contribution of photoelectric effect by using higher atomic number elements [69]. The difference between mass

attenuation of X-ray by different materials are given in Figure 4.1.1.1. As can be seen in the figure, at higher photon energies, the difference of attenuation coefficients of materials is diminished. Thanks to instinct contrast between bones and surrounding soft tissues, bone structures are visualized successfully under X-ray imaging system.

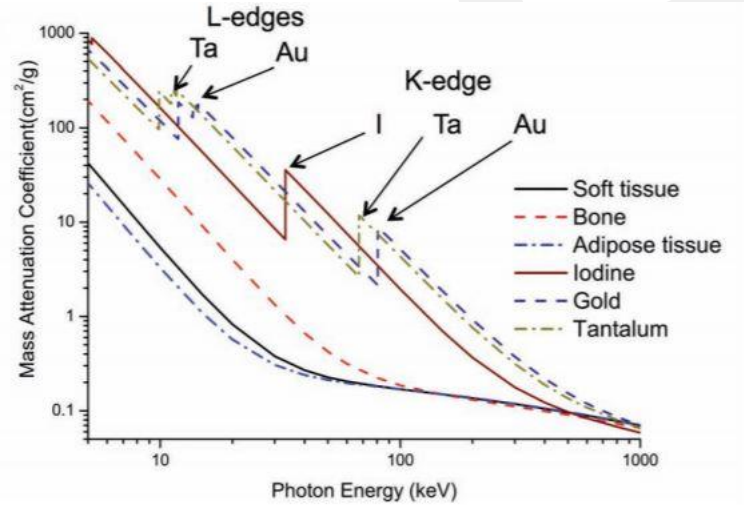

Figure 4.1.1.1 Mass attenuation coefficients of different materials according to X-ray energy [16].

The attenuation coefficients of different soft tissues are relatively close to each also close to the water as can be seen from Figure 4.1.1.2. This is not surprising because the soft tissues mainly made up of water. Iodine has higher attenuation coefficient than water also soft tissue [19]. In unenhanced X-ray imaging, soft tissues that have similar attenuation coefficients cannot be distinguished accurately. Thereby, injecting contrast agents into patient body increases the accuracy of differentiating the tissues with similar coefficients.

The heavy metals are incorporated in contrast agent to increase CT attenuation difference between interest tissue and surrounding tissue[70]. Table 4.1.1.1 provides several heavy elements and their atomic number with K-shell energies. In conclusion, developing new contrast agents can help to lower the radiation to the patient also increases the sensitivity of CT imaging.

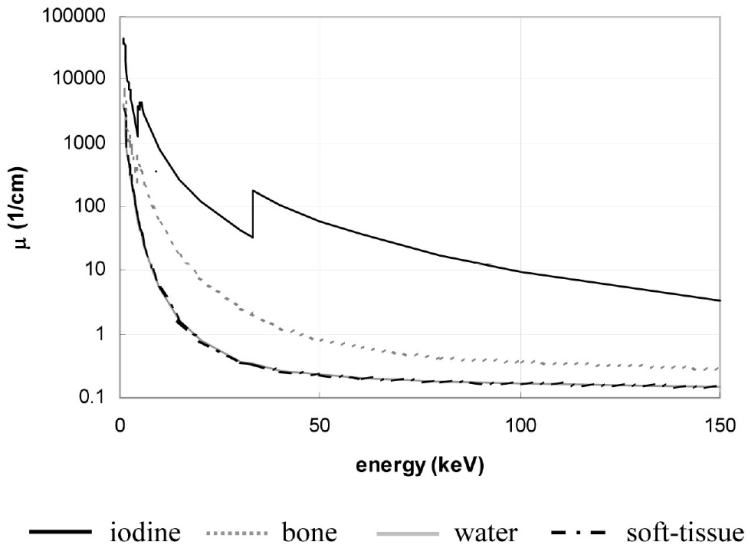

Figure 4.1.1.2 The attenuation coefficients of various materials [19].

Element	Atomic number	K-shell energy
I	53	33.2
Ba	56	37.4
Gd	64	50.2
Tb	65	52.0
Au	79	80.7
Bi	83	90.5

Table 4.1.1.1 Atomic numbers and K-shell energies of several heavy elements [68].

4.2 Related Work

The beginning of contrast agent studies is as early as the development of X-ray imaging modalities. The high atomic number elements such as iodine, barium, bromine, and bismuth were used as contrast agents in early stages of studies. For instance, bismuth was used as a contrast material for the first contrast enhanced angiography on human cadaver [71]. Water-soluble aromatic iodinated molecules

are used currently in biomedical investigations such as angiography, urography and CT imaging [72], [73]. Despite the superior features of iodine-based contrast agents such as high absorption coefficient, chemical tuneability and inertness [73], the efficiency of iodinated contrast agents is degraded by several limitations. For instance, short circulation time of iodine causes rapid clearance of contrast materials from the body. Secondly, higher doses need to be used due to their low contrast enhancement capability [15]. Additionally, non-specific biodistribution of these agents leads to obtaining unclear CT images [16].

To overcome these issues, researchers have started to create new contrast agent formulations. In recent years, great advances in nanotechnology and material science have made an important impact on medical imaging area by developing new generation contrast agents that have ability to overcome many of challenges mentioned above. These agents have opened up new imaging applications through their unique properties.

There exists a numerous number of different nanoparticle types in literature for biomedical investigations and can be divided into two categories as synthetic and natural nanoparticles. The natural nanoparticles such as lipoproteins, viruses, and ferritin are advantageous to synthetic ones due to their biocompatibility and biodegradability [74]. The human-made nanoparticles such as micelles, liposomes, emulsions, metal nanoparticles, silica etc have been studied widely in research area [75]–[77].

The size of synthetic nanoparticle contrast agents varies from 1 to 100 nm and their size can be adjustable in order to reduce renal clearance rate. Gold nanoparticles have been introduced to medical imaging applications and their approaches have been investigated widely. Thanks to their high atomic number, they are excellent to achieve sufficient contrast effect. Additionally, the best range for imaging gold within 80-100 keV. That range decreases the absorption of X-ray by both soft and bone tissues which means radiation dose to the patient can be reduced [78]. A small amount of gold nanoparticle agent administration results in clear imaging of soft tissues owing to larger attenuation coefficient of gold. The

toxicity analysis shows that no sign of toxic effect because of inertness of gold [79].

Bismuth-based nanoparticulate contrast agents have been promising as a new class of contrast agents. When bismuth is compared with gold, bismuth is less expensive and ensures higher contrast enhancement effect. However, fabrication of bismuth-based nanoparticles is difficult [80]. Through the new developments in nanotechnology and material science, capabilities of nanoparticle contrast agents to be improved to address limitations of traditional iodine-based contrast agents.

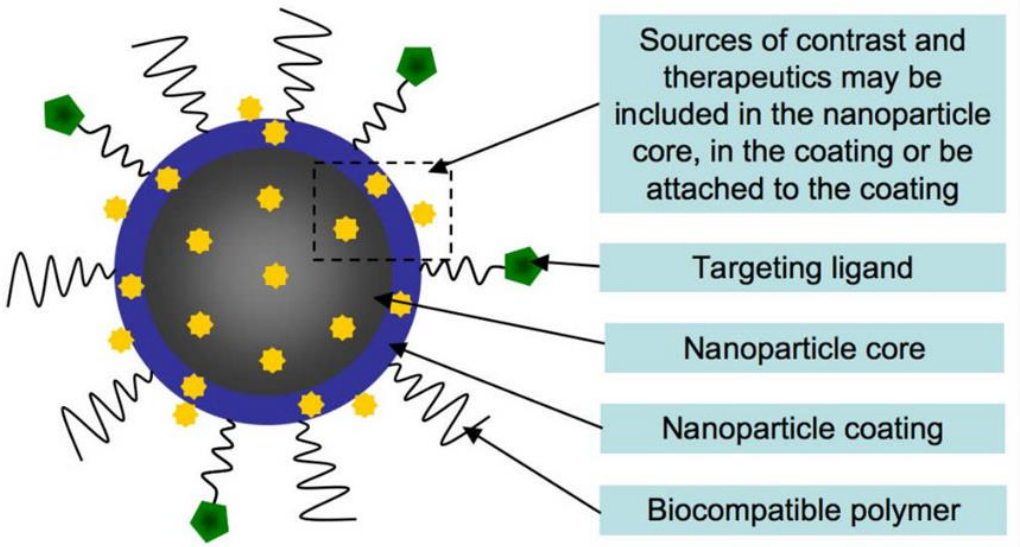

Figure 4.2.1 Typical scheme of a nanoparticle-based contrast agent [75].

In this way, more advanced nanoparticle structures have been introduced to improve the accuracy of imaging techniques also for adding therapeutic features to nanoparticle structures. One of the advanced nanosized structure is magnetic nanoparticles that show magnetic properties and unique physical & chemical properties under certain conditions. They exhibit biocompatible [81] and low toxicity [82] properties in biomedical applications. Magnetic nanoparticles can be divided into three types as ferromagnetic (Fe_2O_3), Maghemite (γ-Fe_2O_3) and paramagnetic. Their fundamental feature is that they can be manipulated under the proper magnetic field. Thus, they can be used in drug delivery applications.

Secondly, they have been utilized as contrast agents in MRI imaging. For instance, one of the most commonly studied magnetic nanoparticle type iron-oxide based magnetic nanoparticles (SPIONs) has been already used in MRI imaging as contrast agents to detect tumours accurately [83]. Also, their targeted drug delivery features have been developed and the results are promising for transporting the drug to disease centre without harming any surrounding tissue [84], [85].

Finally, the greatest advantage of magnetic nanoparticles can be associated with their usage in cancer treatment via hyperthermia. Traditional treatments of cancer include surgery, chemotherapy, and radiation therapy. These traditional therapies have some significant side effects to healthy tissue and also they may lead to tumor recurrence or metastasis since they do not have the capability to rid of all tumorous tissue utterly from the body. At this point, magnetic nanoparticles can provide effective treatment while enhancing the safeness of surrounding healthy tissue. These nanoparticles have potential accumulate and produce sufficient heating to irregular or deep-seated tumor sites when they are exposed to AC magnetic field at proper magnetic strength [86]–[90]. Researchers often use about 100 kHz frequency and 8-16 kA/m magnetic field (H).

However, selecting metal core is a significant factor for reducing health risks of the patient because of toxic considerations. Therefore, iron and manganese are favourable magnetic metals for biomedical applications [91]. However, various metals to utilize as the core of magnetic nanoparticle have been investigated widely.

Previous studies have focused on fabrication of nanoparticle structures and their tuneable compositions. The superiority of nanoparticles on improving the image quality of CT has been indicated through their capability of contrast generation in related papers. According to researchers, the potential of magnetic nanoparticles from the intrinsic physical and chemical properties offers their successful utility on drug delivery and cancer treatment.

4.3 Investigating Contrast Efficacy of Novel Magnetic Nanoparticles for CT Imaging

The present study is intended to investigate the efficiency of novel magnetic nanoparticles as contrast agents for CT imaging. In order to realize this, the experimental setup was designed. In experimental setup, synthetetic CT phantom was formed using agarose gel since it has been used in similar nanoparticle studies. Then, the different ferrofluids containing magnetic nanoparticles (MNPs) were injected to the agarose gel individually. Agarose is a biphasic viscoelastic solid and previous experimental studies showed that higher concentration agarose gels have a structure similar to hard tissue and low concentrations similar to soft tissue [92] thus it is able to mimic biological tissue [93].

The MNPs were fabricated in Mechanical Engineering Department at Istanbul Technical University. MNPs were synthesized as super-paramagnetic NPs (SPIONs) which leads to enable their usage both for contrast enhancement and hyperthermia applications. The MNPs were synthesized with five different cores ($SrFe_xO_y$, $BaFe_xO_y$, $MnFe_xO_y$, $MgFe_xO_y$, and Fe_xO_y).

4.3.1 Experimental Protocol

The steps of the experiment are given in Figure 4.3.1.1. For every sample the same amount of nanofluid (0.1 cc) was injected. After preparation of samples, the coronal CT images were obtained with two different slice thicknesses. Then, the images were displayed using Radiant and MATLAB programs. In order to compare pixel index numbers of reference images (without injection of nanofluid) and different type of MNPs, a pre-processing step was applied.

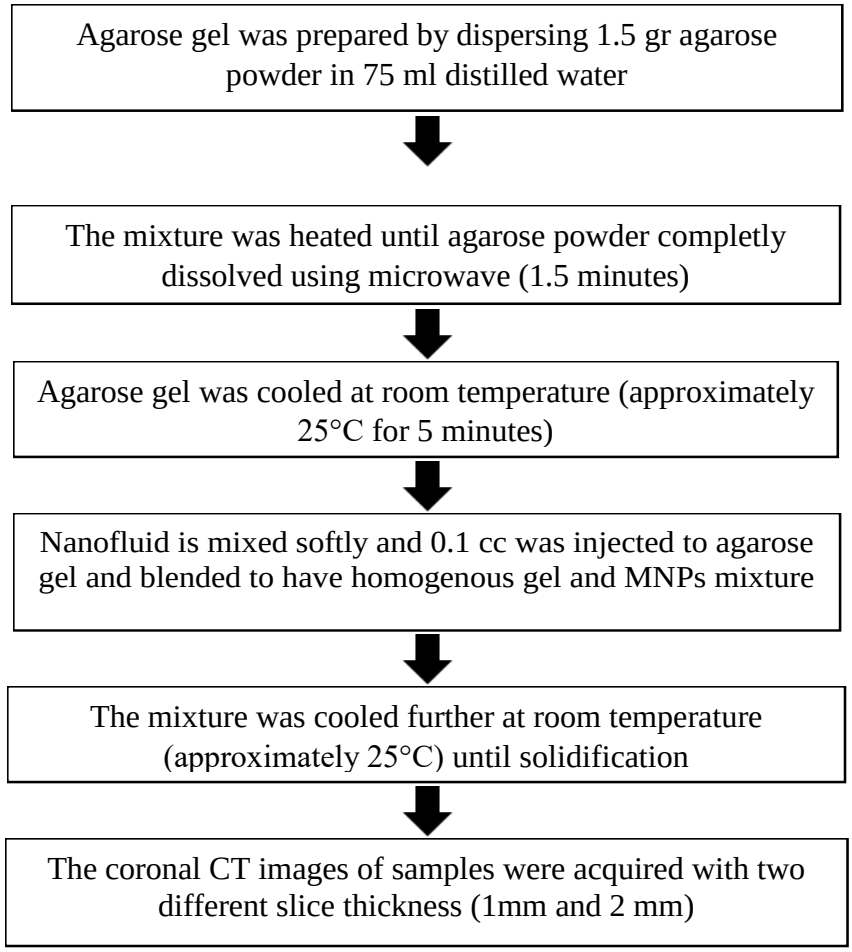

Figure 4.3.1.1 The flow of experiment's steps.

4.3.2 Pre-processing of CT Images

This procedure helped to find the region that includes only agarose gel combined with nanofluid while getting rid of redundant components existing in DICOM images. A result of the pre-processing step is provided in Figure 4.3.2.1. Firstly, each individual image was converted into grayscale. Then, morphological opening operations were applied with the proper structural element to remove protrusions and other redundant components in the images. Morphological operations such as opening and closing are commonly performed in image processing field for noise suppressing, smoothing and filling gaps purposes [94].

Then, the result of morphological operation image was converted into a binary image using proper threshold. The threshold was calculated by using well-known Otsu's global thresholding method [94]. Finally, original DICOM images were multiplied by their binary image to have pure agarose gel and nanofluid mixture region.

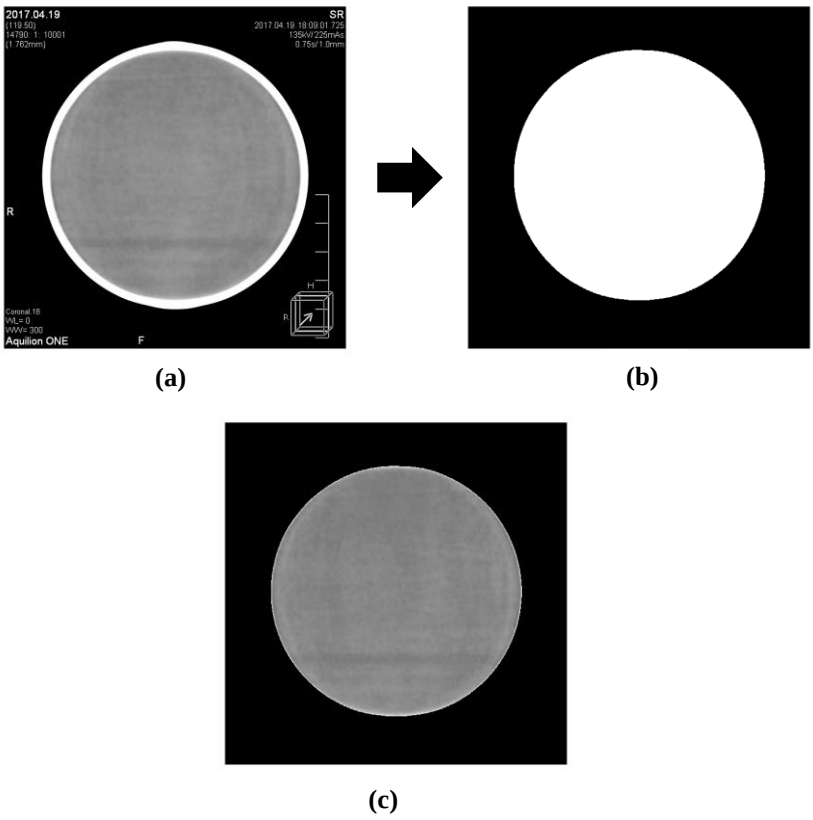

(a) **(b)**

(c)

Figure 4.3.2.1 (a) The main steps of pre-processing beginning with original DICOM image, (b) generated binary image after morphological and thresholding operations and (c) pre-processed image.

4.3.3 Results

In this study, we aim to evaluate the utility of different type MNPs as contrast agents for CT imaging. In order to execute this, the mean pixel intensity values and horizontal pixel intensity profiles were calculated. The total slice

numbers and slices used in the calculation of mean pixel intensity value are provided in Table 4.3.3.1.

The result of mean pixel intensity values is given in Figure 4.3.3.1. The results confirm that adding nanoparticles in agarose gel increases the pixel index number and the MNPs appears brighter in the CT images. According to mean intensity values, Mn and Mg NPs have better X-ray attenuation property and Sr is the second, then respectively Ba and Fe NPs. As expected, the mean intensity value of reference is the lowest while close to Fe NPs.

Samples	Total number of slices	Slices used in calculation of mean pixel intensity values
Reference	32	15, 16, 17
Ba	47	23, 24, 25
Fe	35	16, 17, 18
Mg	39	19, 20, 21
Mn	47	23, 24, 25
Sr	38	18, 19, 20

Table 4.3.3.1: The total slice numbers and the slices used in the calculation of mean intensity value.

Figure 4.3.3.2 illustrates the effect of nanoparticle-fluid on pixel index number along with the horizontal direction at middle same row. The lines of profiles permit to understand how the nanoparticle type affects the pixel index numbers at same slice and at the same row. Despite the same volume of nanofluid was used in each specimen, the horizontal profiles and mean intensity values are quite different. As is seen in the figure, after injection nanofluid the pixel intensity values are increased. The superiority of Sr and Ba NPs are validated against Fe NPs due to their higher pixel index number enhancement. Surprisingly, the

increment of pixel numbers using Fe nanofluid is not as well as other types of NPs while Fe based NPs are commercially used in clinical applications.

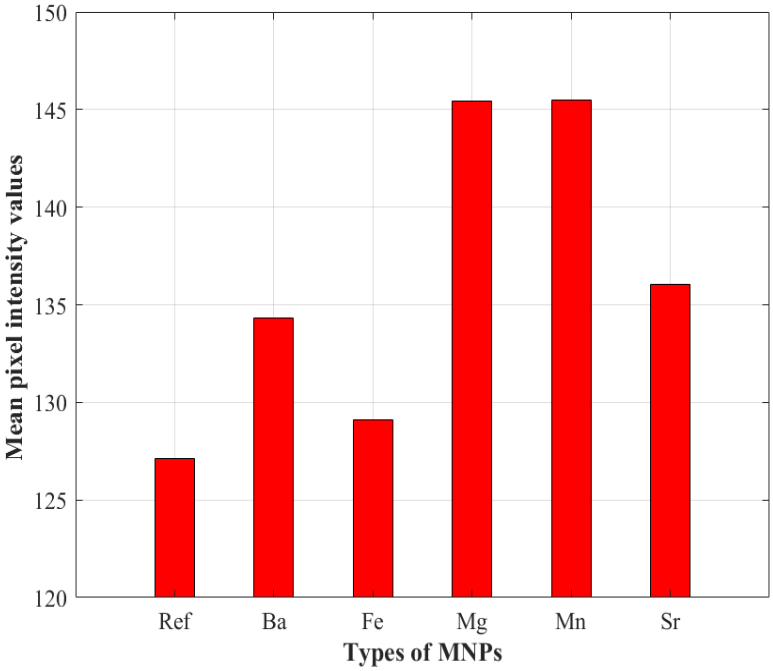

Figure 4.3.3.1 The mean intensity values of the different samples.

Figure 4.3.3.3 illustrates the greatest contrast enhancement of both Mg and Mn-based nanofluids in pixel numbers. Additionally, the profile lines of Mg and Mn are compared with Fe to approve the strongest contrast enhancement capability of both Mg and Mn NPs against to commercially used Fe-core NPs.

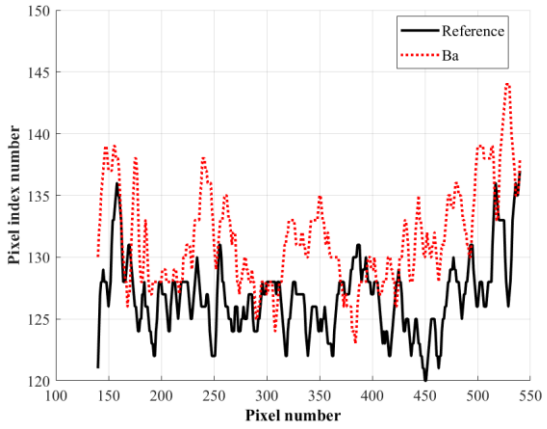

(a)

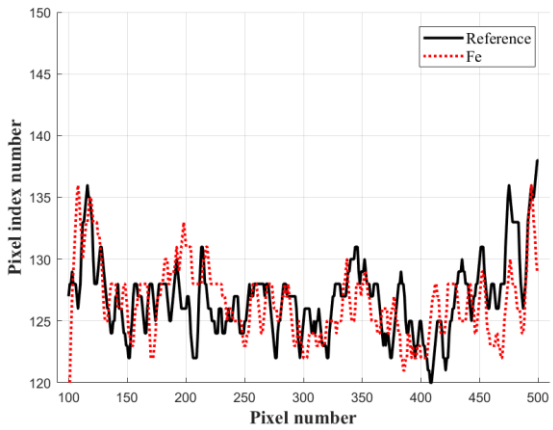

(b)

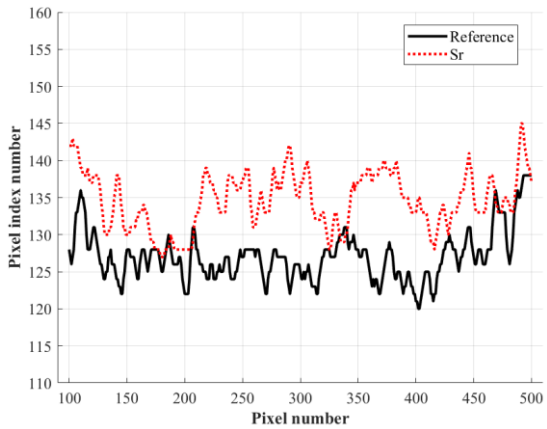

(c)

Figure 4.3.3.2 Horizontal intensity profile comparisons at central slice in between reference and (a) Ba MNPs, (b) Fe MNPs, (c) Sr MNPs at central slice.

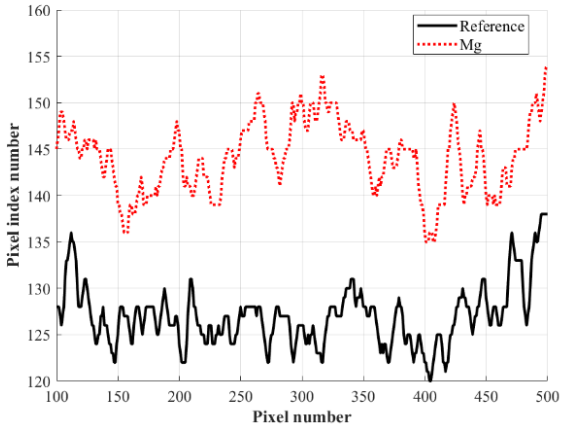

(a)

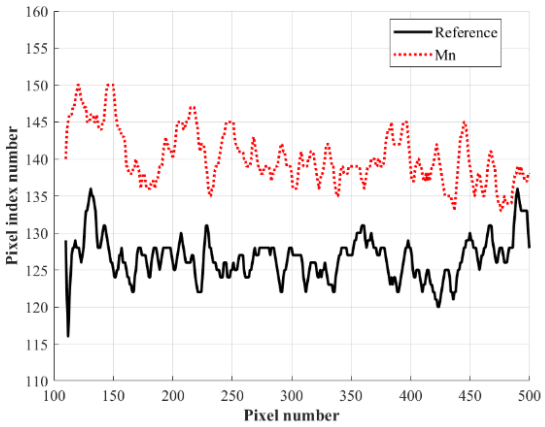

(b)

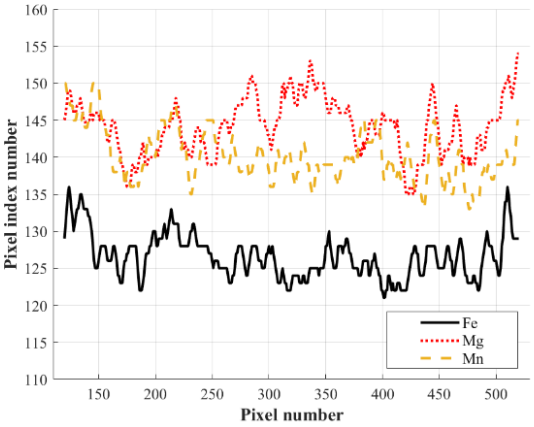

(c)

Figure 4.3.3.3 Horizontal intensity profile comparisons at central slice in between reference and (a) Mg MNPs, (b) Mn MNPs, (c) Fe, Mg, Mn MNPs at central slice.

4.3.4 Discussion and Outlook

As is discussed in this Chapter, there have been great advances in nanoparticle contrast agents for CT imaging in recent years. The fascinating features of nanoparticle contrast agents against to traditional molecular contrast agents permit to improve accuracy of CT imaging. Moreover, specific forms of NPs have been developed such as magnetic-core based nanoparticles recently. With current advancements, MNPs have been utilized as "theranostics" by combining their usage in cancer diagnosis and hyperthermia.

The study attempts to shed light improving CT sensitivity and imaging accuracy using novel MNPs contrast agents. Under the experimental setup as described in the present Chapter, the MNPs are investigated as contrast agents for CT imaging. Since the contrast effect is usually associated with HU numbers for CT imaging, we expect increment on pixel index numbers after injection of the novel MNPs to the agarose gel. The MNPs contrast agents show high X-ray absorption by increasing HU numbers and their performances are superior to Fe NPs which are commercially used. It is found that Mn and Mg cores have superiority in all comparisons. Although the reason behind performance differences of five different core types cannot be explained completely, the MNPs can be suitable choices for more detailed CT images to increase diagnosing accuracy.

However, a few MNPs formulations approved by FDA due to biocompatibility and considerations of possible side effects that can be observed from the administration of MNPs to patient. Since detailed knowledge about degradation, toxic and metabolism process of heavy metals in the human body are not well known, intensive assessment of these procedures is needed.

As the limitations of MNPs contrast agents are addressed, nano-scale contrast agents will be a key component in the field of improving diagnostic imaging capabilities by incorporating active and passive targeting methods. Moreover, their unique properties under proper magnetic field push the MNPs into cancer treatment applications.

Chapter 5

Conclusion and Future Work

In this dissertation, we aimed to improve CT image quality by developing new reconstruction algorithm and increasing the contrast sensitivity of CT imaging system using the novel contrast agents in order to diagnose cancerous tissues more accurately with acceptable radiation dose.

Indeed, there is a trade-off between the image quality and radiation dose. The current CT systems employ traditional FBP that has the ability to reconstruct images at sufficient quality using a high number of projections. However, the high radiation exposure may result in cancer in long-term. Thus, the advanced methods need to be developed to overcome data insufficiency problems. Most of the researchers have been suppressing the image quality degradation by using iterative methods. Iterative methods estimate the image through generating the projection data from the estimated image and comparing it with real projection data. Then, the error term is back propagated to the previous estimated image. The practical application of iterative methods is restricted because of high computation complexity of these methods.

The first contribution of the present thesis is the proposed algorithm for increasing the quality of reconstructed images by using FBP based method to decrease required computation time. However, the major problem in low dose CT imaging is data incompleteness thus FBP significantly degrade image quality. In this case, TV minimization is able to suppress several artifacts arose from a limited number of projections while preserving boundaries of objects in the

image. The developed method combines striking features of these two methods as powerful reconstruction algorithm in order to solve data insufficiency and time limitation problems. The performance of the proposed method was investigated using well known 2D Modified Shepp-Logan phantom. The visual comparisons such as horizontal and vertical profiles have been used. We also informed four quality metrics as RMSE, SNR, CNR, and SSIM to measure numerically the accuracy of the proposed method. The results indicate the superiority of the proposed method against to traditional FBP. Moreover, the outputs of the proposed method are comparable with ART [59] whereas the proposed method reduces computation time greatly. Since FBP is still used in commercial CT scanners, our proposed algorithm can be applied to practice.

The selection of FBP reconstruction parameters has a significant impact on the image quality. The development of adaptive selection of parameters will be one of the future work. The other future work is to test our algorithm with real phantoms.

The second contribution of the thesis centers on approving the usage of novel MNPs as contrast agents for CT imaging. The use of contrast agents in CT imaging has been increased due to inability to differentiate soft tissues from surrounding tissue accurately. This limits the diagnosing accuracy of CT imaging system. Thus, administration of contrast media to enhance the contrast of CT images can help to have more detailed images. In accordance with this purpose, we investigated the contrast efficiency of novel MNPs for CT imaging. MNPs have been studied widely in biomedical applications due to their unique physical and chemical properties. In addition to their superior features against to traditional iodine-based contrast agents, they have therapeutic characteristics.

In order to examine contrast ability of the five different core types MNPs, the experimental protocol was designed. The results of image processing steps indicate the superiority of Mg and Mn magnetic core NPs against to Sr, Ba, and Fe respectively.

Since the MNPs have a theranostic characteristic, they can produce acceptable heating to the cancerous site to remove a tumor utterly from the body

without any damage to surrounding healthy tissues. The utilizing MNPs for hyperthermia will be another future direction of this study.

BIBLIOGRAPHY

[1] L. Fass, “Imaging and cancer: A review,” *Molecular Oncology*, vol. 2, no. 2. pp. 115–152, 2008.

[2] National Center for Health Statistics, “Health, United States, 2016: With Chartbook on Long-term Trends in Health,” *Cent. Dis. Control*, pp. 314–317, 2017.

[3] B. Huang, M. W.-M. Law, and P.-L. Khong, “Whole-body PET/CT scanning: estimation of radiation dose and cancer risk.,” *Radiology*, vol. 251, no. 1, pp. 166–174, 2009.

[4] U. J. Schoepf, C. R. Becker, B. M. Ohnesorge, and E. K. Yucel, “CT of Coronary Artery Disease,” *Radiology*, vol. 232, no. 1, pp. 18–37, 2004.

[5] J. Salimi, K. Bakhtavar, M. Solimani, P. Khashayar, A. P. Meysamie, and M. Zargar, “Diagnostic accuracy of CT scan in abdominal blunt trauma,” *Chin. J. Traumatol.*, vol. 12, no. 2, pp. 67–70, 2009.

[6] D. J. Brenner and E. J. Hall, “Computed tomography--an increasing source of radiation exposure,” *N. Engl. J. Med.*, vol. 357, no. 22, pp. 2277–2284, 2007.

[7] L. Yu *et al.*, “Radiation dose reduction in computed tomography: techniques and future perspective,” *Imaging …*, vol. 1, no. 1, pp. 65–84, 2009.

[8] United Nations Scientific Committee on the Effects of Atomic Radiation, “SOURCES AND EFFECTS OF IONIZING RADIATION,” 2000.

[9] E. J. Hall and D. J. Brenner, “Cancer risks from diagnostic radiology,” *Br. J. Radiol.*, vol. 81, no. 965, pp. 362–378, 2008.

[10] RadiologyInfo.org, “Radiation Dose in X-Ray and CT Exams What are x-rays and what do they do ?,” *Radiologyinfo.Org*, pp. 1–8, 2014.

[11] A. B. De González and S. Darby, “Risk of cancer from diagnostic X-rays: Estimates for the UK and 14 other countries,” *Lancet*, vol. 363, no. 9406,

pp. 345–351, 2004.

[12] R. Doll and R. Peto, “The causes of cancer: Quantitative estimates of avoidable risks of cancer in the united states today,” *J. Natl. Cancer Inst.*, vol. 66, no. 6, pp. 1192–1308, 1981.

[13] P. Oskoui and H. Stark, “A Comparative Study of Three Reconstruction Methods for a Limited-View Computer Tomography Problem,” *IEEE Transactions on Medical Imaging*, vol. 8, no. 1. pp. 43–49, 1989.

[14] E. Y. Sidky, C.-M. Kao, and X. Pan, “Accurate image reconstruction from few-views and limited-angle data in divergent-beam CT,” *J. Xray. Sci. Technol.*, vol. 14, pp. 119–139, 2009.

[15] Y. Liu, K. Ai, and L. Lu, “Nanoparticulate X-ray computed tomography contrast agents: From design validation to in vivo applications,” *Acc. Chem. Res.*, vol. 45, no. 10, pp. 1817–1827, 2012.

[16] N. Lee, S. H. Choi, and T. Hyeon, “Nano-sized CT contrast agents,” *Advanced Materials*, vol. 25, no. 19. pp. 2641–2660, 2013.

[17] F. Wetenschappen and D. Fysica, “Iterative reconstruction for mobile chest tomosynthesis Iteratieve reconstructie voor mobiele tomosynthese van de thorax,” 2016.

[18] T. Buzug, *Computed tomography: From photon statistics to modern cone-beam CT*. .

[19] J. Hsieh, *Computed tomography : principles, design, artifacts, and recent advances*, Second Edi. Bellingham, Washington: SPIE and John Wiley & Sons, Inc, 2009.

[20] G. Michael, “X-ray computed tomography,” *Journals Phys. Educ.*, vol. Special Fe, pp. 442–451, 2001.

[21] C. Tomography, *Webb’s Physics of Medical Imaging*, vol. 51, no. 13. 2006.

[22] “Siemens - SOMATOM Force.” [Online]. Available: https://health.siemens.com/CT_applications/somatom_force/. [Accessed: 08-Jun-2018].

[23] J. Radon, “On the determination of functions from their integrals along certain manifolds,” *Berichte über die Verhandlungen der Sächsische Akad.*

der Wissenschaften, vol. 69, pp. 262–277, 1917.

[24] P. R. Edholm and G. T. Herman, "Linograms in Image Reconstruction from Projections," *IEEE Trans. Med. Imaging*, vol. 6, no. 4, pp. 301–307, 1987.

[25] D. H. Garces, W. T. Rhodes, and N. M. Peña, "Projection-slice theorem: a compact notation," *J. Opt. Soc. Am. A*, vol. 28, no. 5, p. 766, 2011.

[26] J. Fessler, "Analytical tomographic image reconstruction methods," *Image Reconstr. Algorithms Anal.*, p. 3.1-3.47, 2009.

[27] R. L. Siddon, "Fast calculation of the exact radiological path for a three dimensional CT array," *Medical Physics*, vol. 12, no. 2. pp. 252–255, 1985.

[28] J. Hsieh, B. Nett, Z. Yu, K. Sauer, J.-B. Thibault, and C. Bouman, "Recent advances in CT image reconstruction," *Curr. Radiol. Rep.*, vol. 1, pp. 39–51, 2013.

[29] X. Pan, E. Y. Sidky, and M. Vannier, "Why do commercial CT scanners still employ traditional, filtered back-projection for image reconstruction?," *Inverse Probl.*, vol. 25, no. 12, p. 1230009, 2009.

[30] M. Lyra and A. Ploussi, "Filtering in SPECT image reconstruction," *International Journal of Biomedical Imaging*, vol. 2011. 2011.

[31] M. Beister, D. Kolditz, and W. a Kalender, "Iterative reconstruction methods in X-ray CT.," *Phys. Med.*, vol. 28, no. 2, pp. 94–108, 2012.

[32] S. Kaczmarz, "Angenäherte Auflösung von Systemen linearer Gleichungen (Approximate Solution for Systems of Linear Equations)," *Bull. Int. l'Académie Pol. des Sci. des Lettres. Cl. des Sci. Mathématiques Nat. Série A, Sci. Mathématiques*, vol. 35, pp. 355–357, 1937.

[33] R. Gordon, R. Bender, and G. T. Herman, "Algebraic reconstruction techniques (ART) for three-dimensional electron microscopy and x-ray photography.," *J. Theor. Biol.*, vol. 29, no. 3, pp. 471–481, 1970.

[34] H. NYQUIST, "Certain Topics in Telegraph Transmission Theory," *Trans. Am. Inst. Electr. Eng.*, vol. 47, no. 2, pp. 617–644, 1928.

[35] C. E. Shannon, "Communication in the Presence of Noise," *Proc. IRE*, vol. 37, no. 1, pp. 10–21, 1949.

[36] E. J. Candes and M. B. Wakin, “An Introduction To Compressive Sampling,” *IEEE Signal Process. Mag.*, vol. 25, no. 2, pp. 21–30, 2008.

[37] S. Ma, W. Yin, Y. Zhang, and A. Chakraborty, “An efficient algorithm for compressed MR imaging using total variation and wavelets,” *Comput. Vis. Pattern Recognition, 2008. CVPR 2008. IEEE Conf.*, pp. 1–8, 2008.

[38] D. L. Donoho, “For most large underdetermined systems of linear equations the minimal ℓ 1-norm solution is also the sparsest solution,” *Commun. Pure Appl. Math.*, vol. 59, no. 6, pp. 797–829, 2006.

[39] E. J. Candès, J. Romberg, and T. Tao, “Robust uncertainty principles: Exact signal reconstruction from highly incomplete frequency information,” *IEEE Trans. Inf. Theory*, vol. 52, no. 2, pp. 489–509, 2006.

[40] L. I. Rudin, S. Osher, and E. Fatemi, “Nonlinear total variation based noise removal algorithms,” *Phys. D Nonlinear Phenom.*, vol. 60, no. 1–4, pp. 259–268, 1992.

[41] A. M. Cormack, “Representation of a function by its line integrals, with some radiological applications. II,” *J. Appl. Phys.*, vol. 35, no. 10, pp. 2908–2913, 1964.

[42] P. R. Smith, T. M. Peters, and R. H. T. Bates, “Image reconstruction from finite numbers of projections,” *J. Phys. A Gen. Phys.*, vol. 6, no. 3, pp. 361–382, 1973.

[43] H. Shi and S. Luo, “A novel scheme to design the filter for CT reconstruction using FBP algorithm,” *Biomed. Eng. Online*, vol. 12, no. 1, 2013.

[44] J. Shtok, M. Elad, and M. Zibulevsky, “Adaptive filtered-back-projection for Computed Tomography,” in *IEEE Convention of Electrical and Electronics Engineers in Israel, Proceedings*, 2008, pp. 528–532.

[45] D. M. Pelt and K. J. Batenburg, “Improving filtered backprojection reconstruction by data-dependent filtering,” *IEEE Trans. Image Process.*, vol. 23, no. 11, pp. 4750–4762, 2014.

[46] S. Horbelt, M. Liebling, and M. Unser, “Filter design for filtered back-projection guided by the interpolation model,” *Proc. SPIE*, no. August

2015, pp. 806–813, 2002.

[47] C. Schretter, C. Neukirchen, G. Rose, and M. Bertram, “Optimal Pre-Filtering for Linear Interpolation in Computed Tomography,” pp. 1–4.

[48] C. Mu and C. Park, “Optimal Filtered Backprojection for Fast and Accurate Tomography Reconstruction,” no. Xx, pp. 1–12, 2016.

[49] H. Shi, S. Luo, Z. Yang, and G. Wu, “A novel iterative CT reconstruction approach based on FBP algorithm,” *PLoS One*, vol. 10, no. 9, 2015.

[50] J. G. Colsher, “Iterative three-dimensional image reconstruction from tomographic projections,” *Comput. Graph. Image Process.*, vol. 6, no. 6, pp. 513–537, 1977.

[51] A. H. Andersen and A. C. Kak, “Simultaneous algebraic reconstruction technique (SART): A superior implementation of the art algorithm,” *Ultrason. Imaging*, vol. 6, no. 1, pp. 81–94, 1984.

[52] M. Goitein, “Three-dimensional density reconstruction from a series of two-dimensional projections,” *Nucl. Instruments Methods*, vol. 101, no. 3, pp. 509–518, 1972.

[53] E. T. Quinto, “Tomographic reconstructions from incomplete data - Numerical inversion of the exterior Radon transform,” *Inverse Probl.*, vol. 4, no. 3, pp. 867–876, 1988.

[54] X. Jin, L. Li, Z. Chen, L. Zhang, and Y. Xing, “Anisotropic total variation for limited-angle CT reconstruction,” in *IEEE Nuclear Science Symposium Conference Record*, 2010, pp. 2232–2238.

[55] Y. Yang, L. Li, and Z. Chen, “3D Anisotropic Total Variation method for Limited- angle CT Reconstruction,” no. 3, pp. 1–4, 2013.

[56] X. Liu and L. Huang, “A new nonlocal total variation regularization algorithm for image denoising,” *Math. Comput. Simul.*, vol. 97, pp. 224–233, 2014.

[57] H. Xu, Q. Sun, N. Luo, G. Cao, and D. Xia, “Iterative Nonlocal Total Variation Regularization Method for Image Restoration,” *PLoS One*, vol. 8, no. 6, 2013.

[58] H. Kim, J. Chen, A. Wang, C. Chuang, M. Held, and J. Pouliot, “Non-local

total-variation (NLTV) minimization combined with reweighted L1-norm for compressed sensing CT reconstruction," *Phys. Med. Biol.*, vol. 61, no. 18, pp. 6878–6891, 2016.

[59] M. Ertas, A. Akan, I. Yildirim, and M. Kamasak, "Sparse tomographic image reconstruction method using total variation and non-local means," in *IST 2015 - 2015 IEEE International Conference on Imaging Systems and Techniques, Proceedings*, 2015.

[60] T. Farquhar and A. Chatziioannou, "An investigation of filter choice for filtered back-projection reconstruction in PET," *Nucl. Sci. ...*, vol. 45, no. 3, pp. 0–4, 1997.

[61] S. A. Qureshi, S. M. Mirza, and M. Arif, "Inverse Radon Transform-based image reconstruction using various frequency domain filters in parallel beam transmission tomography," in *2005 Student Conference on Engineering Sciences and Technology, SCONEST*, 2005.

[62] A. M. Mota, N. Matela, N. Oliveira, and P. Almeida, "Total variation minimization filter for DBT imaging," *Med. Phys.*, vol. 42, no. 6, pp. 2827–2836, 2015.

[63] L. A. Shepp and B. F. Logan, "The Fourier reconstruction of a head section," *IEEE Transactions on Nuclear Science*, vol. 21, no. 3. pp. 21–43, 1974.

[64] a. M. Eskicioglu and P. S. Fisher, "Image quality measures and their performance," *IEEE Trans. Commun.*, vol. 43, no. 12, pp. 2959–2965, 1995.

[65] Z. Wang, A. C. Bovik, H. R. Sheikh, and E. P. Simoncelli, "Image quality assessment: From error visibility to structural similarity," *IEEE Trans. Image Process.*, vol. 13, no. 4, pp. 600–612, 2004.

[66] M. Ertas, I. Yildirim, M. Kamasak, and A. Akan, "Iterative image reconstruction using non-local means with total variation from insufficient projection data," *J Xray Sci Technol*, 2016.

[67] L. W. Goldman, "Principles of CT and CT Technology," *J. Nucl. Med. Technol.*, vol. 35, no. 3, pp. 115–128, 2007.

[68] S.-B. Yu and A. D. Watson, “Metal-Based X-ray Contrast Media,” *Chem. Rev.*, vol. 99, no. 9, pp. 2353–2378, 1999.

[69] D. Pan *et al.*, “Computed tomography in color: Nanok-enhanced spectral CT molecular imaging,” *Angew. Chemie - Int. Ed.*, vol. 49, no. 50, pp. 9635–9639, 2010.

[70] H. Lusic and M. W. Grinstaff, “X-ray-computed tomography contrast agents,” *Chemical Reviews*, vol. 113, no. 3. pp. 1641–1666, 2013.

[71] M. K. Kassabian, “Roentgen_rays_and_electro_therapeutics.pdf.” p. 671, 1907.

[72] C. Christiansen, “X-ray contrast media—an overview,” *Toxicology*, vol. 209, no. 2, pp. 185–187, 2005.

[73] W. Krause and P. W. Schneider, *Contrast Agents I*, vol. 221, no. January 2002. 2002.

[74] D. P. Cormode, P. A. Jarzyna, W. J. M. Mulder, and Z. A. Fayad, “Modified natural nanoparticles as contrast agents for medical imaging,” *Advanced Drug Delivery Reviews*, vol. 62, no. 3. pp. 329–338, 2010.

[75] D. P. Cormode, T. Skajaa, Z. A. Fayad, and W. J. M. Mulder, “Nanotechnology in medical imaging: Probe design and applications,” *Arterioscler. Thromb. Vasc. Biol.*, vol. 29, no. 7, pp. 992–1000, 2009.

[76] W. J. M. Mulder, G. J. Strijkers, G. A. F. Van Tilborg, D. P. Cormode, Z. A. Fayad, and K. Nicolay, “Nanoparticulate assemblies of amphiphiles and diagnostically active materials for multimodality imaging,” *Acc. Chem. Res.*, vol. 42, no. 7, pp. 904–914, 2009.

[77] I. I. Slowing, B. G. Trewyn, and V. S. Y. Lin, “Mesoporous silica nanoparticles for intracellular delivery of membrane-impermeable proteins,” *J. Am. Chem. Soc.*, vol. 129, no. 28, pp. 8845–8849, 2007.

[78] J. F. Hainfeld, D. N. Slatkin, T. M. Focella, and H. M. Smilowitz, “Gold nanoparticles: A new X-ray contrast agent,” *Br. J. Radiol.*, vol. 79, no. 939, pp. 248–253, 2006.

[79] D. Kim, S. Park, H. L. Jae, Y. J. Yong, and S. Jon, “Antibiofouling polymer-coated gold nanoparticles as a contrast agent for in vivo X-ray

computed tomography imaging," *J. Am. Chem. Soc.*, vol. 129, no. 24, pp. 7661–7665, 2007.

[80] A. L. Brown and A. M. Goforth, "PH-dependent synthesis and stability of aqueous, elemental bismuth glyconanoparticle colloids: Potentially biocompatible X-ray contrast agents," *Chem. Mater.*, vol. 24, no. 9, pp. 1599–1605, 2012.

[81] R. Weissleder *et al.*, "Superparamagnetic Pharmacokinetics Iron Oxide : and Toxicity," *Am. J. Roentgenol.*, vol. 152, pp. 167–173, 1989.

[82] M. G. Harisinghani *et al.*, "Noninvasive detection of clinically occult lymph-node metastases in prostate cancer.," *N. Engl. J. Med.*, vol. 348, no. 25, pp. 2491–9, 2003.

[83] H. Lee, E. Lee, D. K. Kim, N. K. Jang, Y. Y. Jeong, and S. Jon, "Antibiofouling polymer-coated superparamagnetic iron oxide nanoparticles as potential magnetic resonance contrast agents for in vivo cancer imaging," *J. Am. Chem. Soc.*, vol. 128, no. 22, pp. 7383–7389, 2006.

[84] S. C. McBain, H. H. P. Yiu, and J. Dobson, "Magnetic nanoparticles for gene and drug delivery," *International Journal of Nanomedicine*, vol. 3, no. 2. pp. 169–180, 2008.

[85] M. Shinkai, "Functional magnetic particles for medical application," *Journal of Bioscience and Bioengineering*, vol. 94, no. 6. pp. 606–613, 2002.

[86] A. Ito, K. Tanaka, H. Honda, S. Abe, H. Yamaguchi, and T. Kobayashi, "Complete regression of mouse mammary carcinoma with a size greater than 15 mm by frequent repeated hyperthermia using magnetite nanoparticles.," *J. Biosci. Bioeng.*, vol. 96, no. 4, pp. 364–369, 2003.

[87] M. Johannsen *et al.*, "Clinical hyperthermia of prostate cancer using magnetic nanoparticles: Presentation of a new interstitial technique," *Int. J. Hyperth.*, vol. 21, no. 7, pp. 637–647, 2005.

[88] A. Jordan *et al.*, "The effect of thermotherapy using magnetic nanoparticles on rat malignant glioma," *J. Neurooncol.*, vol. 78, no. 1, pp. 7–14, 2006.

[89] P. Wust *et al.*, "Magnetic nanoparticles for interstitial thermotherapy -

Feasibility, tolerance and achieved temperatures," *Int. J. Hyperth.*, vol. 22, no. 8, pp. 673–685, 2006.

[90] K. Maier-Hauff *et al.*, "Efficacy and safety of intratumoral thermotherapy using magnetic iron-oxide nanoparticles combined with external beam radiotherapy on patients with recurrent glioblastoma multiforme," *J. Neurooncol.*, vol. 103, no. 2, pp. 317–324, 2011.

[91] C. Felton, A. Karmakar, Y. Gartia, P. Ramidi, A. S. Biris, and A. Ghosh, "Magnetic nanoparticles as contrast agents in biomedical imaging: Recent advances in iron- and manganese-based magnetic nanoparticles," *Drug Metabolism Reviews*, vol. 46, no. 2. pp. 142–154, 2014.

[92] R. K. Jain, "Transport of Molecules, Particles, and Cells in Solid Tumors," *Annu. Rev. Biomed. Eng.*, vol. 1, no. 1, pp. 241–263, 1999.

[93] L. Aranda-Lara, E. Torres-García, and R. Oros-Pantoja, "Biological Tissue Modeling with Agar Gel Phantom for Radiation Dosimetry of ^{99m}Tc," *Open J. Radiol.*, vol. 04, no. 01, pp. 44–52, 2014.

[94] R. Gonzalez and R. Woods, *Digital image processing*. 2002.